INTERNATIONAL JOURNAL FOR NUMERICAL METHODS IN FLUIDS
Int. J. Numer. Meth. Fluids 2000; **34**: 241–275

Three-dimensional boundary element analysis of drop deformation in confined flow for Newtonian and viscoelastic systems

Roger E. Khayat*,[1]

Department of Mechanical and Materials Engineering, The University of Western Ontario, London, Ontario, Canada N6A 5B9

SUMMARY

An adaptive (Lagrangian) boundary element approach is proposed for the general three-dimensional drop deformation in confined flow. The adaptive method is stable as it includes remeshing capabilities of the deforming interface between drop and suspending fluid, and thus can handle large deformations. Both drop and surrounding fluid are viscous incompressible and can be Newtonian or viscoelastic. A boundary-only formulation is implemented for fluids obeying the linear Jeffrey's constitutive equation. Similarly to the formulation for two-dimensional Newtonian fluids (Khayat RE, Luciani A, Utracki LA. Boundary element analysis of planar drop deformation in confined flow. Part I. Newtonian fluids. *Engineering Analysis of Boundary Elements* 1997; **19**: 279), the method requires the solution of two simultaneous integral equations on the interface between the two fluids and the confining solid boundary. Although the problem is formulated for any confining geometry, the method is illustrated for a deforming drop as it is driven by the ambient flow inside a cylindrical tube. The accuracy of the method is assessed by comparison with the analytical solution for two-phase radial spherical flow, leading to good agreement. The influence of mesh refinement is examined for a drop in simple shear flow.

KEY WORDS: boundary element; 3D; drop deformation; viscoelastic systems

1. INTRODUCTION

This study is concerned with the three-dimensional drop deformation of a single drop as it is subjected to the action of the ambient flow inside a channel. The boundary element method (BEM) is extended to treat both Newtonian and viscoelastic systems. Extensive studies have been carried for two-dimensional deformation. The two-dimensional modeling imposes limits on the physical description of the problem. For example, the droplets are modeled as infinite

* Correspondence to: Department of Mechanical and Materials Engineering, Faculty of Engineering Sciences, University of Western Ontario, London, Ontario, Canada N6A 5B9.
[1] E-mail: rkhayat@eng.uwo.ca

Received March 1999
Revised August 1999

cylinders and no velocity component in the direction transverse to the plane of the channel is taken into account. Aside from its physical and practical significance, the present three-dimensional formulation constitutes a good benchmark to examine the effectiveness of the BEM for multiphase and moving-boundary problems.

The simulation of drop deformation in an ambient flow constitutes a class of problem of the moving-boundary type. For moving-boundary problems, the implementation of conventional numerical approaches, such as the methods of finite elements or finite difference, can often be extremely costly given the requirement for domain remeshing at each time step of the procedure. Remeshing and mesh refinement are easily handled when the BEM is used, even for three-dimensional problems [1–6]. The method offers an obvious advantage when dealing with moving-domain problems as it necessitates only the discretization of the boundary and not that of the inner volume domain. The three-dimensional problem is, therefore, reduced to computing the flow field on the two-dimensional boundary. Thus, the simplicity in implementation of the BEM and its ability to handle complex three-dimensional moving-boundary flows have recently been demonstrated for confined and free surface flows [1–6].

More generally, different approaches may be used for the solution of moving-boundary/initial value problems, but none of them is general enough to simulate all types of moving or free boundary problems. These methods may be classified as Eulerian, Lagrangian, and mixed Eulerian–Lagrangian. However, these (domain) methods have rarely been applied to drop deformation. The principal difficulty with solving moving-boundary problems is that the position of the interface is *a priori* unknown, and must be determined as part of the solution. The BEM relates velocities at points within the fluid to the velocity and stress on the bounding surfaces. It is thus an ideal method for studying moving-boundary problems, such as a drop deformation in another fluid. The advantages of the BEM include the reduction of problem dimensionality, the direct calculation of the interfacial velocity, the ability to track large surface deformations, and the potential for easy incorporation of interfacial tension as well as other surface effects. The BEM has been applied to a number of problems in materials processing of the moving-boundary type. These problems include the transient cavity mixing of Newtonian and viscoelastic fluids [1,2], the flow of a metal in the shot sleeve of die casting machines [3], the transient three-dimensional extrusion [4], the penetration stage during gas-assisted injection molding [5], and the prediction of flow movement during the evacuation of air from the mold during blow molding and thermoforming [6].

The BEM has also been the method of choice for problems of drop deformation. While extensive work has been devoted to the modeling and simulation of drops deforming in an infinite fluid medium, relatively little work has been done in the case of a drop deforming in a confined medium. In both cases, most simulations were carried out using the BEM. Applications of the BEM have ranged from the classical study of a rising drop in an otherwise quiescent medium [7–9] to more complex situations, such as drop break-up and coalescences [10,11], the deformation of biological cells [12,13], and the deformation of small drops in electric and magnetic fields [14]. Some studies also included the influence of non-uniform flow, such as the deformation of drops in shear [15,16] and extensional [17–19] flows. More recently, the BEM has been extended to include the motion of a drop in the vicinity of a plane wall [12,20,21], a deformable interface [22], the deformation of drops in confined flows such as inside a circular channel [23,24], and in a channel with constriction [25]. These latter studies,

however, examined only axisymmetric motion. The drop deformation was, therefore, confined along the axis of the channel. Some work, although very little, dealt with three-dimensional deformation, such as a drop placed in an ambient planar shear wall, and the deformation of a liquid film flowing down an inclined wall over a particle captured by the wall [24]. For additional studies on drop deformation and related works, see References [15,24,26–28].

Using the BEM, Khayat and associates recently assessed the two-dimensional influence of shear and elongation on drop deformation with relevance to mixing [29–34]. Confined flow configurations of both Newtonian and viscoelastic systems were examined, such as a drop deforming in convergent–divergent, purely divergent, and straight channels [29,30]. A boundary element analysis was also carried out to simulate the drop deformation in the screw channel of a mixing extruder [31]. Experiments were carried out in rectangular tubes for drops initially located on and off the tube axis. Good agreement was obtained upon comparison between theory and experiment despite the limiting assumption of two-dimensional analysis [32,33]. A shear- or elongation-dominated drop deformation depends on the size of the drop relative to the channel dimension(s), and its position relative to the axis of the channel. The influence of viscosity ratio and interfacial tension on the drop deformation was also examined. The effects of shear thinning were recently examined for a drop moving in a Newtonian ambient fluid [34]. These studies were, however, limited to two-dimensional flow.

The present paper focuses on the viscoelastic, three-dimensional deformation of a drop inside a duct of arbitrary shape, with emphasis on circular flow. The problem is of industrial and fundamental interests as it concerns mixing and dispersing in multi-component liquid systems. The inherent transient nature of the flow process and the presence of a moving interface make the simulation of the problem challenging because of the non-linearities involved. The challenge becomes even greater if both inertia and non-Newtonian effects are accounted for. Such non-linear phenomena have been addressed in moving-boundary problems with relevance to polymer processing. For instance, viscoelastic effects were examined for the growth of spherical and cylindrical shells of fluids obeying the highly non-linear viscoelastic constitutive model [35]. It was found that, even under constant driving pressure, oscillatory growth results from elastic normal stress effects. In order to assess the mathematical intricacies in the case of pressure-driven flows, Khayat [36] examined the small planar deformation of a viscoelastic column of fluid obeying the upper-convected Maxwell constitutive model by applying a regular perturbation approach. It was found that the governing equations are indeed hyperbolic and, therefore, unlike the Navier–Stokes equations, they can entertain an oscillatory solution for a statically stressed fluid. The same problem was later examined for large deformations using the finite element method [37]. Non-linear effects, such as those stemming from fluid elasticity, fluid inertia, or the high rate of deformation of the interface or free surface, are difficult to account for in a boundary element approach despite the advent of recent techniques to handle non-linear and transient problems [28,38,39].

For non-linear viscoelastic problems, the BEM traditionally requires the discretization of a volume integral, which includes all the non-linear terms in the form of a pseudo-body force [40,41]. In this case, the major advantage of the BEM is lost as a result of the inner volume discretization. More recent techniques, such as the methods of dual- and multiple-reciprocity, have been developed to transform the volume integral into a boundary integral. Although these methods still require the evaluation of the flow field at internal points, they do not

require the discretization of the inner domain, and the BEM retains its major advantage. However, the capability of such techniques to handle highly non-linear problems, such as flows with strong inertia or (elastic) normal stress effects, remains questionable [28,38,39,42,43].

In this study, inertia and non-linear viscoelastic (convective) effects are assumed negligible. Both drop and suspending fluid obey the linear Oldroyd-B or Jeffrey's equation [44]. Typically, existing BEM formulations for linear viscoelastic problems are carried out in the frequency domain [45–47]. The boundary integral equations in the current study are obtained and solved in the time domain. The derivation of the boundary integral equation for viscoelastic flow is based on the Laplace transform of the flow variables. The association of the integral transform of the viscoelastic solution with that associated with the Newtonian flow problem is similar to the correspondence principle for linear viscoelastic solids or the elastico-viscoelastic analogy [48,49]. Although the derivation given here uses the Laplace transform, an analogous procedure follows from the use of the Fourier transform. Read [50] was the first to recognize this association through the Fourier transform, while Sips [51], Brull [52], and Lee [53] gave the corresponding Laplace transform results. The present procedure consists of replacing the viscosity by the appropriate form in the transformed equations and reinterpreting the transformed flow variables as transformed viscoelastic field variables. The transformed equations are then solved and the solution is inverted to obtain the evolution of the flow field with time. In the present work, however, the inversion is avoided and the boundary integral equations are derived in the time domain. A time-marching scheme is then implemented for the discretization of the time derivatives and the solution of the integral equations.

The paper is organized as follows. The governing equations, boundary and initial conditions are discussed in Section 2. The boundary integral equations for two-phase viscoelastic flow are derived in Section 3. The numerical implementation and solution procedure are covered in Section 4. Numerical assessment of the method and results on the influence of fluid properties on drop deformation is given in Section 5. Concluding remarks are given in Section 6.

2. GOVERNING EQUATIONS, BOUNDARY AND INITIAL CONDITIONS

In this section, a general formulation of the boundary integral equations for viscoelastic fluids obeying the Jeffrey's constitutive model is presented. These equations are then applied to the deformation of a drop in a confined medium. Only low-Reynolds number flows, typically characterized by small velocities, small length scales, and/or high viscosity, will be considered. In this limit, the inertia terms in the momentum equation are negligible, so the flow is in a state of creeping motion.

2.1. Governing equations

At any instant of time, t, the drop, which occupies a three-dimensional region, $\Omega_d(t)$, is assumed to be neutrally buoyant so the effects of gravity and any external body forces are neglected. The suspending fluid occupies the outer region, $\Omega_s(t)$, and is driven by an imposed pressure gradient, traction, or movement of the outer boundary of the confining channel. The situation is typically illustrated in Figure 1. The regions $\Omega_s(t)$ and $\Omega_d(t)$ are assumed separated

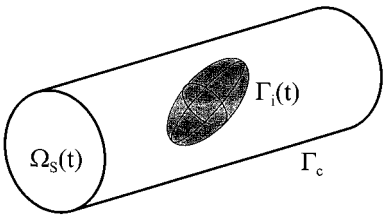

Figure 1. Schematic of flow configuration for drop deformation inside a confining duct. Two-phase system consists of suspending fluid region, $\Omega_s(t)$ bounded by $\Gamma_s(t) = \Gamma_c \cup \Gamma_i(t)$, and drop region, $\Omega_d(t)$ bounded by $\Gamma_i(t)$.

at all times by a moving interface, $\Gamma_i(t)$. Thus, situations where the drop comes in contact with the boundary of the duct, Γ_c, and drop break-up are excluded. The region $\Omega_s(t)$ is always bounded by $\Gamma_i(t)$ and Γ_c; it is thus convenient to introduce $\Gamma_s(t) = \Gamma_i(t) \cup \Gamma_c$ as the boundary of $\Omega_s(t)$. The conservation of mass and momentum equations in each region may be written as

$$\nabla \cdot \mathbf{u}_\alpha(\mathbf{x}, t) = 0, \qquad \nabla \cdot \boldsymbol{\sigma}_\alpha(\mathbf{x}, t) = \mathbf{0}, \quad \mathbf{x} \in \Omega_\alpha(t) \cup \Gamma_\alpha(t) \tag{1}$$

with the subscript $\alpha = \mathrm{d}$ or s, corresponding to a variable in the drop or suspending fluid region respectively. Here, ∇ is the gradient operator, $\mathbf{x}$ is the position vector, $\mathbf{u}_\alpha(\mathbf{x}, t)$ is the velocity vector, and $\boldsymbol{\sigma}_\alpha(\mathbf{x}, t)$ is the total stress tensor. This latter term is given in terms of the hydrostatic pressure $p_\alpha(\mathbf{x}, t)$ and excess stress tensor $\mathbf{S}_\alpha(\mathbf{x}, t)$, such that

$$\boldsymbol{\sigma}_\alpha(\mathbf{x}, t) = -p_\alpha(\mathbf{x}, t)\mathbf{I} + \eta_\alpha \mathbf{S}_\alpha(\mathbf{x}, t), \quad \mathbf{x} \in \Omega_\alpha(t) \cup \Gamma_\alpha(t) \tag{2}$$

where η_α is the viscosity of the fluid and $\mathbf{I}$ is the identity tensor. The acceleration term $\partial \mathbf{u}_\alpha / \partial t$ in the momentum conservation equation is neglected, so that for a Newtonian fluid, the formulation in question is not strictly unsteady but quasi-steady. This quasi-steady state assumption is valid whenever $L^2/v_\alpha \ll T$, where L and T are typical characteristic length and time of the flow respectively, and v_α is the kinematic viscosity. In the present case, $T \sim L/U$, where U is a typical value of the driving velocity. Thus, for the quasi-steady state assumption to apply, one must have the Reynolds number $Re = UL/v_\alpha \ll 1$. This is indeed typically the case for fluids of interest to mixing problems involving high-viscosity fluids. Physically, the quasi-steady state approximation means that a Newtonian fluid immediately adjusts to changes in the movement of the boundary or boundary conditions. This is not necessarily the case for a viscoelastic fluid.

Although the flow is expected to be significantly influenced by the constitutive model, the choice of a suitable model for $\mathbf{S}_\alpha(\mathbf{x}, t)$ is not critical in the present study. The study's major objective is to investigate the influence of fluid elasticity on an already complex flow behavior as it arises for Newtonian fluids alone. It is then more prudent to adopt as simple a viscoelastic constitutive equation as possible. Moreover, the assumption of linear constitutive behavior makes the approach inadequate to handle highly non-linear viscoelastic phenomena. Thus,

although large strains are present in the flows examined here, only small strain rates are assumed to be involved, making the usually important non-linearities in the constitutive equation rather negligible. Such non-linearities typically stem from convective and upper-convective terms, and the dependence of viscosity and relaxation time on shear and elongation rates. In this study, the constitutive equation for $\mathbf{S}_\alpha(\mathbf{x}, t)$ is taken to correspond to the Jeffrey's model [44]

$$\lambda_\alpha^{(1)}\dot{\mathbf{S}}_\alpha(\mathbf{x}, t) + \mathbf{S}_\alpha(\mathbf{x}, t) = \eta_\alpha \lfloor \boldsymbol{\Delta}_\alpha(\mathbf{x}, t) + \lambda_\alpha^{(2)}\dot{\boldsymbol{\Delta}}_\alpha(\mathbf{x}, t) \rfloor, \quad \mathbf{x}\in\Omega_\alpha(t)\cup\Gamma_\alpha(t) \tag{3}$$

where $\lambda_\alpha^{(1)}$ and $\lambda_\alpha^{(2)}$ $(0 \le \lambda_\alpha^{(2)} < \lambda_\alpha^{(1)})$ are the relaxation and retardation times of the fluid occupying $\Omega_\alpha(t)$ respectively, and $\boldsymbol{\Delta}_\alpha(\mathbf{x}, t) \equiv \nabla\mathbf{u}_\alpha(\mathbf{x}, t) + \nabla\mathbf{u}_\alpha^t(\mathbf{x}, t)$ is the rate-of-strain tensor. Note that an overdot denotes partial differentiation with respect to time. Despite its simplicity, the Jeffrey's model is known to be adequate to describe the rheology of polymer solutions [44]. Typically, the solution is composed of a polymer solute in a Newtonian solvent, with viscosity $\eta_\alpha^{(p)}$ and $\eta_\alpha^{(s)}$ respectively. It is then convenient to express $\mathbf{S}_\alpha(\mathbf{x}, t)$ as a sum of Newtonian and elastic contributions, such that

$$\mathbf{S}_\alpha(\mathbf{x}, t) = \eta_\alpha\Delta_\alpha(\mathbf{x}, t) + \tau_\alpha(\mathbf{x}, t) \tag{4}$$

where $\tau_\alpha(\mathbf{x}, t)$ is the elastic part of the stress tensor. In this case, the governing equations for $\mathbf{u}_\alpha(\mathbf{x}, t)$, $p_\alpha(\mathbf{x}, t)$, and $\tau_\alpha(\mathbf{x}, t)$ follow from Equations (1)–(4), and may be written here as

$$\nabla\cdot\mathbf{u}_\alpha(\mathbf{x}, t) = 0 \tag{5}$$

$$\nabla\cdot\tau_\alpha(\mathbf{x}, t) + \eta_\alpha^{(s)}\nabla^2\mathbf{u}_\alpha(\mathbf{x}, t) - \nabla p_\alpha(\mathbf{x}, t) = \mathbf{0}, \quad \mathbf{x}\in\Omega_\alpha(t)\cup\Gamma_\alpha(t) \tag{6}$$

$$\lambda_\alpha^{(1)}\dot{\tau}_\alpha(\mathbf{x}, t) + \tau_\alpha(\mathbf{x}, t) = \eta_\alpha^{(p)}\Delta_\alpha(\mathbf{x}, t) \tag{7}$$

In this case, the retardation time is related to the relaxation time and the polymer-to-solvent viscosity ratio

$$\lambda_\alpha^{(2)} = \frac{\lambda_\alpha^{(1)}\eta_\alpha^{(s)}}{\eta_\alpha^{(s)} + \eta_\alpha^{(p)}} = \frac{\lambda_\alpha^{(1)}}{1 + (\eta_\alpha^{(p)}/\eta_\alpha^{(s)})} \tag{8}$$

The viscosity of the fluid in region $\Omega_\alpha(t)$ becomes simply the sum of the solvent and solute viscosities: $\eta_\alpha = \eta_\alpha^{(s)} + \eta_\alpha^{(p)}$. In the limit $\eta_\alpha^{(s)} \to 0$, Equations (6) and (7) reduce to the equations corresponding to Maxwell flow or polymer melt. The Newtonian limit is recovered if, further, $\lambda_\alpha^{(1)} \to 0$.

2.2. Boundary conditions

While the boundary conditions on Γ_c are straightforward to implement, those on $\Gamma_i(t)$ must be examined more closely. The fluid is assumed to adhere to the solid boundary, so that stick boundary conditions apply on Γ_c. More generally, the velocity is assumed to be fully

prescribed on Γ_c. At the entrance and exit of the channel, the fluid is assumed to obey Poiseuille flow. The velocity boundary condition may then, conveniently, be written in the following compact form:

$$\mathbf{u}_s(\mathbf{x}, t) = \mathbf{u}_c(\mathbf{x}), \quad \mathbf{x} \in \Gamma_c \tag{9}$$

Thus, the flow field is determined through Equations (1) and (2) for each fluid medium, and is subject to condition (9) on Γ_c, and dynamic and kinematic conditions on $\Gamma_i(t)$. The proper choice and implementation of the latter is not obvious [54].

In this paper, the interface is assumed to deform pointwise along the normal, $\mathbf{n}(\mathbf{x}, t)$, with the normal projection of the fluid velocity at the interface. This method keeps the points evenly distributed on the interface. Thus, the following kinematic boundary condition holds on $\Gamma_i(t)$:

$$\frac{d\mathbf{x}}{dt} = \mathbf{n}(\mathbf{x}, t)[\mathbf{n}(\mathbf{x}, t) \cdot \mathbf{u}(\mathbf{x}, t)], \quad \mathbf{x} \in \Gamma_i(t) \tag{10}$$

Here $\mathbf{n}$ is the normal unit vector at the interface directed from the suspending fluid region to the region occupied by the drop. A Lagrangian approach, such as the one involving the solution of Equation (10), requires usually remeshing or mesh refinement of the free surface. Remeshing is relatively easily handled by the BEM, given the lower dimension of the boundary relative to domain methods.

The dynamic condition at the interface is based on the continuity of the tangential stress and discontinuity of normal stress caused by the interfacial tension. Let $\mathbf{t}_\alpha(\mathbf{x}, t) = \boldsymbol{\sigma}_\alpha(\mathbf{x}, t) \cdot \mathbf{n}(\mathbf{x}, t)$ be the traction so that the dynamic condition becomes

$$\mathbf{t}_s(\mathbf{x}, t) - \mathbf{t}_d(\mathbf{x}, t) = \gamma \kappa(\mathbf{x}, t) \mathbf{n}(\mathbf{x}, t), \quad \mathbf{x} \in \Gamma_i(t) \tag{11a}$$

where $\kappa(\mathbf{x}, t)$ is the local curvature and γ is the interfacial tension coefficient. Note that boundary condition (11a) is derived under conditions of equilibrium and uniform interfacial tension. Its validity under dynamic conditions is simply assumed [55]. The continuity of velocity also applies at the interface so that

$$\mathbf{u}_s(\mathbf{x}, t) = \mathbf{u}_d(\mathbf{x}, t) \equiv \mathbf{u}_i(\mathbf{x}, t), \quad \mathbf{x} \in \Gamma_i(t) \tag{11b}$$

where the velocity at the interface is conveniently defined as $\mathbf{u}_i(\mathbf{x}, t)$.

2.3. Initial conditions

As to the initial conditions, the fluid is assumed to be initially at rest, or more particularly, in a stress-free state

$$\mathbf{u}_\alpha(\mathbf{x}, t = 0) \equiv \mathbf{0}, \qquad \mathbf{t}_\alpha(\mathbf{x}, t = 0) = \mathbf{0}, \quad \mathbf{x} \in \Omega_\alpha(t = 0) \cup \Gamma_\alpha(t = 0) \tag{12}$$

The assumption of initial equilibrium may seem incompatible with the assumption that the acceleration term in the momentum equation is negligible. This is certainly true if the initial

jump in the boundary condition(s) is significant. However, since the viscosity of the fluid is high and the imposed velocity is typically low, the assumption of negligible acceleration, even initially, may still be valid. Conditions (12) greatly simplify the solution procedure for the viscoelastic flow as will be seen below.

3. BOUNDARY INTEGRAL FORMULATION

In this section, the boundary integral equation is derived for the general viscoelastic flow of the linear Oldroyd-B type. Emphasis is placed on two-phase flow. The numerical solution procedure and time-marching scheme are also described.

3.1. Generalized boundary integral equation for two-phase viscoelastic flow

While the formalism behind the BEM for Stokes flow is well-established [24,28], that corresponding to viscoelastic fluids is relatively unexplored. Given the linearity of the constitutive equation (4), the governing equations can be Laplace transformed. The problem reduces to that corresponding to Stokes flow in the frequency domain. The Voltera principle in the frequency domain, which is also known as the correspondence principle [26–28], allows the solution of a boundary value problem in viscoelasticity to be obtained from the solution of the corresponding Newtonian problem, with the viscosity being replaced by a transformed characteristic of the fluid. The final boundary integral equation is obtained in the time domain.

The first step in the procedure consists of taking the Laplace transform of the governing equations (5)–(7). Since the fluid is incompressible, the transformed continuity and momentum equations retain the same form in the frequency domain

$$\nabla\cdot\bar{\mathbf{u}}_\alpha(\mathbf{x}, s) = 0 \tag{13}$$

$$\nabla\cdot\bar{\tau}_\alpha(\mathbf{x}, s) + \eta_\alpha^{(s)}\nabla^2\bar{\mathbf{u}}_\alpha(\mathbf{x}, s) - \nabla\bar{p}_\alpha(\mathbf{x}, s) = \mathbf{0}, \quad \mathbf{x}\in\Omega_\alpha\cup\Gamma_\alpha \tag{14}$$

where an overbar on the velocity or stress variable designates Laplace transformation. An expression for the transformed excess stress is also obtained from Equation (7) in terms of the transformed rate-of-strain tensor, $\bar{\Gamma}_\alpha(\mathbf{x}, s)$, which is mathematically equivalent to Newton's law of viscosity

$$\bar{\tau}_\alpha(\mathbf{x}, s) = \frac{\eta_\alpha^{(p)}}{\lambda_\alpha^{(1)}+1}\bar{\Gamma}_\alpha(\mathbf{x}, s) \equiv \frac{\eta_\alpha^{(p)}}{\lambda_\alpha^{(1)}+1}[\nabla\mathbf{u}_\alpha(\mathbf{x}, s) + \nabla\mathbf{u}_\alpha^t(\mathbf{x}, s)] \tag{15}$$

If Equation (15) is inserted in Equation (14), and Equation (13) is used, then the momentum equation in the frequency domain takes the same form as for Stokes flow

$$\bar{\eta}_\alpha\nabla^2\bar{\mathbf{u}}_\alpha(\mathbf{x}, s) - \nabla\bar{p}_\alpha(\mathbf{x}, s) = \mathbf{0}; \quad \bar{\eta}_\alpha = \frac{1}{\lambda_\alpha^{(1)}s+1}\eta_\alpha \tag{16}$$

Note that an equivalent viscosity, $\bar{\eta}_\alpha$, is now obtained, which is a function of the Laplace parameter s. The solution procedure for the problem in the frequency domain proceeds similarly to the case of the flow of a Newtonian fluid [24,28]. In order to derive the integral representation for Equations (13) and (16), the fundamental solution for the problem is needed. This singular solution corresponds to the velocity and stress fields at a point $\mathbf{x}$ produced by a point force $\bar{\mathbf{F}}(s)\delta(\mathbf{x}-\mathbf{y})$ located at $\mathbf{y}$, where δ is the Dirac delta function. In this case, the acting force is generally a function of the parameter s, and therefore depends on time. For a viscoelastic fluid, this also corresponds to the same force that acts initially at time $t=0$. In other words, the force in real time is given by $\mathbf{F}\delta(\mathbf{x}-\mathbf{y})\delta(t)$. Denoting the singular solution variables with asterisks, and taking the Laplace transform of the viscoelastic equations over the infinite medium, the problem reduces to that corresponding to Stokes flow in the frequency domain

$$\nabla\cdot\bar{\mathbf{u}}^*_\alpha(\mathbf{x}|\mathbf{y},s)=0, \qquad \nabla\cdot\bar{\boldsymbol{\sigma}}^*_\alpha(\mathbf{x}|\mathbf{y},s)=\bar{\mathbf{F}}(s)\delta(\mathbf{x}-\mathbf{y}) \tag{17a}$$

where $\bar{\boldsymbol{\sigma}}^*_\alpha(\mathbf{x}|\mathbf{y},s)=-\bar{p}^*_\alpha(\mathbf{x}|\mathbf{y},s)\mathbf{I}+\bar{\eta}_\alpha\bar{\boldsymbol{\Gamma}}^*_\alpha(\mathbf{x}|\mathbf{y},s)$, with the following boundary conditions:

$$|\bar{\mathbf{u}}^*_\alpha(\mathbf{x}|\mathbf{y},s)|\to 0, \qquad |\bar{\boldsymbol{\sigma}}^*_\alpha(\mathbf{x}|\mathbf{y},s)|\to 0 \quad \text{as} \quad |\mathbf{x}|\to\infty \tag{17b}$$

This yields the following expressions for the transformed velocity $\bar{\mathbf{u}}^*_\alpha(\mathbf{x}|\mathbf{y},s)$ and stress $\bar{\boldsymbol{\sigma}}^*_\alpha(\mathbf{x}|\mathbf{y},s)$, namely

$$\bar{\mathbf{u}}^*_\alpha(\mathbf{x}|\mathbf{y},s)=\frac{\lambda^{(1)}_\alpha s+1}{\eta_\alpha}\,\mathbf{J}(\mathbf{x}|\mathbf{y})\cdot\bar{\mathbf{F}}(s), \qquad \bar{\boldsymbol{\sigma}}^*_\alpha(\mathbf{x}|\mathbf{y},s)=\mathbf{K}(\mathbf{x}|\mathbf{y})\cdot\bar{\mathbf{F}}(s) \tag{18}$$

The kernels, or Green's functions, $\mathbf{J}$ and $\mathbf{K}$ are second- and third-rank tensors respectively, and are given by

$$\mathbf{J}(\mathbf{x}|\mathbf{y})=\frac{1}{8\pi}\left(\frac{\mathbf{I}}{r}+\frac{\mathbf{rr}}{r^3}\right), \qquad \mathbf{K}(\mathbf{x}|\mathbf{y})=\frac{3}{4\pi}\frac{\mathbf{rrr}}{r^4} \tag{19}$$

for an unbounded three-dimensional domain, where $\mathbf{r}=\mathbf{x}-\mathbf{y}$ and $\mathbf{r}=|\mathbf{x}-\mathbf{y}|$. Note that $\mathbf{J}$ and $\mathbf{K}$ are respectively, second-rank symmetric and third-rank anti-symmetric tensors with respect to $\mathbf{r}$. The corresponding integral representation is now derived similar to that corresponding to Stokes flow. The Reciprocal (Green's) theorem is first invoked, relating the fields $(\bar{\mathbf{u}}_\alpha,\bar{\boldsymbol{\sigma}}_\alpha)$ and $(\bar{\mathbf{u}}^*_\alpha,\bar{\boldsymbol{\sigma}}^*_\alpha)$. The theorem is straightforward to derive [28], and its statement for the present problem is as follows:

$$\begin{aligned}&\int_{\Omega_\alpha(t)}\{\bar{\mathbf{u}}_\alpha(\mathbf{y},s)\cdot\lfloor\nabla_{\mathbf{y}}\cdot\bar{\boldsymbol{\sigma}}^*_\alpha(\mathbf{x}|\mathbf{y},s)\rfloor-\bar{\mathbf{u}}^*_\alpha(\mathbf{x}|\mathbf{y},s)\cdot[\nabla_{\mathbf{y}}\cdot\bar{\boldsymbol{\sigma}}_\alpha(\mathbf{y},s)]\}\,\mathrm{d}\Omega_{\mathbf{y}}\\&=\int_{\Gamma_\alpha(t)}\mathbf{n}(\mathbf{y},t)\cdot[\bar{\boldsymbol{\sigma}}^*_\alpha(\mathbf{x}|\mathbf{y},s)\cdot\bar{\mathbf{u}}_\alpha(\mathbf{y},s)-\bar{\boldsymbol{\sigma}}_\alpha(\mathbf{y},s)\cdot\bar{\mathbf{u}}^*_\alpha(\mathbf{x}|\mathbf{y},s)]\,\mathrm{d}\Gamma_{\mathbf{y}}\end{aligned} \tag{20}$$

where s is just a parameter. Substitution of the fundamental singular solution (18) into theorem (20), using Equation (17), removing the arbitrary vector $\bar{\mathbf{F}}$, and interchanging the label $\mathbf{x}$ and $\mathbf{y}$, lead to the following integral equation in the frequency domain:

$$\int_{\Gamma_\alpha(t)} \mathbf{n}(\mathbf{y})\cdot\left[\left(\frac{\lambda_\alpha^{(1)}s+1}{\eta_\alpha}\right)\bar{\boldsymbol{\sigma}}(\mathbf{y},s)\cdot\mathbf{J}(\mathbf{x}|\mathbf{y})\right]\mathrm{d}\Gamma_\mathbf{y} - \int_{\Gamma_\alpha(t)} \mathbf{n}(\mathbf{y},t)\cdot[\bar{\mathbf{u}}(\mathbf{y},s)\cdot\mathbf{K}(\mathbf{x}|\mathbf{y})]\,\mathrm{d}\Gamma_\mathbf{y}$$
$$= c_\alpha(\mathbf{x},t)\bar{\mathbf{u}}_\alpha(\mathbf{x},s), \quad \mathbf{x}\in\Omega_\alpha(t)\cup\Gamma_\alpha(t) \tag{21}$$

where $c_\alpha(\mathbf{x},t)$ is equal to 1 for $\mathbf{x}$ belonging to the interior of $\Omega_\alpha(t)$. For a point on the boundary $\Gamma_\alpha(t)$, its value depends on the jump in the value of the first integral on the boundary as the boundary is crossed. Thus $c_\alpha(\mathbf{x},t)=\frac{1}{2}$ if the boundary is Lyapunov smooth, which requires that a local tangent to the boundary exists everywhere. This assumption, however, is not valid in the vicinity of sharp corners, cusps, or edges. In such cases, a separate treatment is needed. This issue will be further examined shortly.

The inverse Laplace transform of Equation (21) yields the desired integral equation in the time domain

$$\frac{1}{\eta_\alpha}\int_{\Gamma_\alpha(t)} \mathbf{n}(\mathbf{y},t)\cdot\left[\lambda_\alpha^{(1)}\frac{\partial\boldsymbol{\sigma}_\alpha(\mathbf{y},t)}{\partial t}+\boldsymbol{\sigma}_\alpha(\mathbf{y},t)\right]\cdot\mathbf{J}(\mathbf{x}|\mathbf{y})\,\mathrm{d}\Gamma_\mathbf{y} - \int_{\Gamma_\alpha(t)} \mathbf{n}(\mathbf{y},t)\cdot\mathbf{u}_\alpha(\mathbf{y},t)\cdot\mathbf{K}(\mathbf{x}|\mathbf{y})\,\mathrm{d}\Gamma_\mathbf{y}$$
$$= c_\alpha(\mathbf{x},t)\mathbf{u}_\alpha(\mathbf{y},t), \quad \mathbf{x}\in\Omega_\alpha(t)\cup\Gamma_\alpha(t) \tag{22}$$

for the class of problems envisaged in the present study.

In the derivation of Equation (22), the fluids are tacitly assumed to be in a state of rest initially, or, more particularly, in a stress-free state. As mentioned earlier, this assumption greatly simplifies the formulation. Indeed, the inclusion of an initial stress condition leads to an additional term in Equation (15) when the Laplace transform of the constitutive equation (7) is taken. If the initial stress is not generally a constant, thus is dependent on position, a volume integral emerges, which must be added to the integral equation (21) in the frequency domain. Correspondingly, a volume integral emerges in Equation (22) in the time domain. It is obvious that the presence of a volume integral complicates matters significantly, and may not be necessary for a wide range of practical flow problems.

In the limit $\lambda_\alpha^{(1)}\to 0$, Equation (22) reduces to the integral equation corresponding to Stokes flow

$$\frac{1}{\eta_\alpha}\int_{\Gamma_\alpha(t)} \mathbf{t}_\alpha(\mathbf{y},t)\cdot\mathbf{J}(\mathbf{x}|\mathbf{y})\,\mathrm{d}\Gamma_\mathbf{y} - \int_{\Gamma_\alpha(t)} \mathbf{n}(\mathbf{y},t)\cdot\mathbf{u}_\alpha(\mathbf{y},t)\cdot\mathbf{K}(\mathbf{x}|\mathbf{y})\,\mathrm{d}\Gamma_\mathbf{y} = c_\alpha(\mathbf{x},t)\mathbf{u}_\alpha(\mathbf{y},t),$$
$$\mathbf{x}\in\Omega_\alpha(t)\cup\Gamma_\alpha(t) \tag{23}$$

Unlike Equation (22), Equation (23) relates directly the velocity field $\mathbf{u}_\alpha(\mathbf{x},t)$ at any point inside the fluid region $\Omega_\alpha(t)$, or on the boundary $\Gamma_\alpha(t)$, to the traction $\mathbf{t}_\alpha(\mathbf{x},t)$. The situation is quite different for the viscoelastic flow problem. The major difficulty in dealing with the solution of Equation (22) is the explicit presence of the stress tensor rather than the traction

vector as in Equation (23). Equation (22) is valid for the general transient viscoelastic flow with moving boundary, where the normal to the boundary changes with time. A direct relation between velocity and traction is not possible unless the normal vector is constant with time.

Consider now the evaluation of $c_\alpha(\mathbf{x}, t)$ for $\mathbf{x}$ belonging to $\Gamma_\alpha(t)$. At each time, t, the value of $c_\alpha(\mathbf{x}, t)$ depends solely on the geometry of the boundary involved. Thus, $c_\alpha(\mathbf{x}, t) = \frac{1}{2}$ for a smooth boundary. More generally, if a uniform velocity field, such as $\mathbf{u}_\alpha(\mathbf{x}, t) = u\mathbf{e}$, is applied over a closed boundary, $\mathbf{e}$ being the direction of the velocity and u its magnitude, then all derivatives (including tractions and stresses) must vanish. Hence, at any time t, Equation (22) reduces to

$$c_\alpha(\mathbf{x}, t) = \mathbf{ee}: \int_{\Gamma_\alpha(t)} [\mathbf{n}(\mathbf{y}, t)\cdot\mathbf{K}(\mathbf{x}|\mathbf{y})]\, d\Gamma_\mathbf{y}, \quad \mathbf{x}\in\Gamma_\alpha(t) \tag{24}$$

This expression for $c_\alpha(\mathbf{x}, t)$ can be used at each time step of the flow, as the fluid is moving to occupy a changing domain.

3.2. Boundary integral equations for drop deformation

It is convenient to apply Equation (22) separately to the two regions occupied by the drop and the suspending fluid. First, recall that for the present problem $\Omega_\alpha(t) \equiv \Omega_\mathrm{d}(t)$ and $\Gamma_\alpha(t) \equiv \Gamma_\mathrm{i}(t)$ for the fluid occupying the drop region, and $\Omega_\alpha(t) \equiv \Omega_\mathrm{s}(t)$ and $\Gamma_\alpha(t) \equiv \Gamma_\mathrm{s}(t) \equiv \Gamma_\mathrm{i}(t) \cup \Gamma_\mathrm{c}$ for the suspending fluid, so that Equation (22) may be explicitly written as

$$\frac{1}{\eta_\mathrm{s}}\int_{\Gamma_\mathrm{i}(t)} \mathbf{n}(\mathbf{y}, t)\cdot\left[\lambda_\mathrm{s}\frac{\partial\boldsymbol{\sigma}_\mathrm{s}(\mathbf{y}, t)}{\partial t} + \boldsymbol{\sigma}_\mathrm{s}(\mathbf{y}, t)\right]\cdot\mathbf{J}(\mathbf{x}|\mathbf{y})\, d\Gamma_\mathbf{y} + \frac{1}{\eta_\mathrm{s}}\int_{\Gamma_\mathrm{c}}\left[\lambda_\mathrm{s}\frac{\partial\mathbf{t}_\mathrm{s}(\mathbf{y}, t)}{\partial\mathbf{t}} + \mathbf{t}_\mathrm{s}(\mathbf{y}, t)\right]\cdot\mathbf{J}(\mathbf{x}|\mathbf{y})\, d\Gamma_\mathbf{y}$$

$$-\int_{\Gamma_\mathrm{i}(t)} \mathbf{n}(\mathbf{y}, t)\cdot\mathbf{u}_\mathrm{i}(\mathbf{y}, t)\cdot\mathbf{K}(\mathbf{x}|\mathbf{y})\, d\Gamma_\mathbf{y} = \int_{\Gamma_\mathrm{c}} \mathbf{n}(\mathbf{y})\cdot\mathbf{u}_\mathrm{c}(\mathbf{y})\cdot\mathbf{K}(\mathbf{x}|\mathbf{y})\, d\Gamma_\mathbf{y} + \begin{cases} \mathbf{u}_\mathrm{s}(\mathbf{y}, t) & \mathbf{x}\in\Omega_\mathrm{s}(t) \\ c_\mathrm{s}(\mathbf{x}, t)\mathbf{u}_\mathrm{s}(\mathbf{y}, t) & \mathbf{x}\in\Gamma_\mathrm{c} \\ c_\mathrm{s}(\mathbf{x}, t)\mathbf{u}_\mathrm{i}(\mathbf{y}, t) & \mathbf{x}\in\Gamma_\mathrm{i}(t) \\ \mathbf{0} & \mathbf{x}\in\Omega_\mathrm{d}(t) \end{cases} \tag{25}$$

when Equation (22) is applied to the suspending fluid region, and

$$\frac{1}{\eta_\mathrm{d}}\int_{\Gamma_\mathrm{i}(t)} \mathbf{n}(\mathbf{y}, t)\cdot\left[\lambda_\mathrm{d}\frac{\partial\boldsymbol{\sigma}_\mathrm{d}(\mathbf{y}, t)}{\partial t} + \boldsymbol{\sigma}_\mathrm{d}(\mathbf{y}, t)\right]\cdot\mathbf{J}(\mathbf{x}|\mathbf{y})\, d\Gamma_\mathbf{y} - \int_{\Gamma_\mathrm{i}(t)} \mathbf{n}(\mathbf{y}, t)\cdot\mathbf{u}_i(\mathbf{y}, t)\cdot\mathbf{K}(\mathbf{x}|\mathbf{y})\, d\Gamma_\mathbf{y}$$

$$= \begin{cases} \mathbf{0} & \mathbf{x}\in\Omega_\mathrm{s}(t)\cup\Gamma_\mathrm{c} \\ c_\mathrm{d}(\mathbf{x}, t)\mathbf{u}_\mathrm{d}(\mathbf{y}, t), & \mathbf{x}\in\Gamma_\mathrm{i}(t) \\ \mathbf{u}_\mathrm{d}(\mathbf{y}, t), & \mathbf{x}\in\Omega_\mathrm{d}(t) \end{cases} \tag{26}$$

when Equation (22) is applied to the drop region. Note that the superscript (1) has been dropped from $\lambda_\mathrm{s}^{(1)}$ and $\lambda_\mathrm{d}^{(1)}$. The presence of the traction in the second integral of Equation

(25), as opposed to that of the stress tensor, is due to the fact that the normal vector to the channel boundary, Γ_c, does not depend on time. Note that condition (9) was also used. The evolution of the interface is the main phenomenon of interest to the present problem. The principal variable is thus the velocity at the interface $\mathbf{u}_d(\mathbf{x}\in\Gamma_i, t) = \mathbf{u}_s(\mathbf{x}\in\Gamma_i, t) \equiv \mathbf{u}_i(\mathbf{x}\in\Gamma_i, t)$. Note that the tractions on each side of the interface must also be determined. Condition (11a) may be taken advantage of, which relates the normal tractions in terms of the interfacial tension coefficient, and the tractions are eliminated at the interface. However, unlike the Newtonian case [54], Equations (25) and (26) involve explicitly the stress rather than the traction. This problem will be circumvented once the numerical solution to the problem is examined.

4. SOLUTION PROCEDURE AND NUMERICAL IMPLEMENTATION

In this section, the solution of system (25) and (26) is examined, subject to the kinematic and dynamic conditions at the interface. A time-marching scheme is first implemented for the integral and kinematic equations. At each time, the location of the nodes and elements of the discretized interface is determined by solving Equation (10). As the boundary elements are distorted, the mesh is refined through element subdivision. This allows the stress at the interface to be eliminated by invoking the dynamic condition. Finally, the numerical implementation of the discretized equations is discussed.

4.1. Time-marching scheme

As mentioned above, the principal variable of interest is the velocity at the interface, which dictates the evolution of the drop. For Newtonian fluids [29,30], the tractions on each side of the interface need not be determined. Condition (11a) can be used, which relates the normal tractions in terms of the interfacial tension coefficient, and the tractions can be eliminated at the interface altogether. The situation is more difficult for viscoelastic fluids as the traction at the interface does not figure explicitly in Equations (25) and (26). This difficulty is circumvented by approximating the time derivative of the stress by a finite difference. If a Euler scheme is used and higher-order terms in the time increment Δt are neglected, then

$$\mathbf{n}(\mathbf{y}, t)\cdot\left[\lambda_\alpha \frac{\partial \boldsymbol{\sigma}_\alpha(\mathbf{y}, t)}{\partial t} + \boldsymbol{\sigma}_\alpha(\mathbf{y}, t)\right] \approx \left(\frac{\lambda_\alpha}{\Delta t} + 1\right)\mathbf{t}_\alpha(\mathbf{y}, t) - \frac{\lambda_\alpha}{\Delta t}\,\mathbf{n}(\mathbf{y}, t)\cdot\boldsymbol{\sigma}_\alpha(\mathbf{y}, t-\Delta t) + O(\Delta t) \tag{27}$$

By using Equation (27), the integral equations (25) and (26) will only involve the traction (and not the stress) at the current time. However, the stress $\sigma_\alpha(\mathbf{y}, t-\Delta t)$ must still be dealt with. For this, one can derive an equation for stress similar to that for Newtonian fluids [24,28], which makes the computational requirement much heavier, even if this is done at the post-processing stage. Alternatively, the treatment becomes much simpler if the normal vector at the current time is expanded about the previous time step and higher-order terms in Δt are neglected: $\mathbf{n}(\mathbf{y}, t) \approx \mathbf{n}(\mathbf{y}, t-\Delta t) + O(\Delta t)$. In this case, Equation (27) reduces to

$$\mathbf{n}(\mathbf{y},t)\cdot\left[\lambda_\alpha\frac{\partial\boldsymbol{\sigma}_\alpha(\mathbf{y},t)}{\partial t}+\boldsymbol{\sigma}_\alpha(\mathbf{y},t)\right]\approx\left(\frac{\lambda_\alpha}{\Delta t}+1\right)\mathbf{t}_\alpha(\mathbf{y},t)-\frac{\lambda_\alpha}{\Delta t}\,\mathbf{t}_\alpha(\mathbf{y},t-\Delta t)+O(\Delta t) \tag{28}$$

A similar discretization scheme is also applied to Equation (10) in order to determine the evolution of the interface.

4.2. Boundary element equations

Using the above time discretization, Equation (25) becomes

$$\begin{aligned}&\frac{1}{\eta_s}\int_{\Gamma_c}\mathbf{T}_s(\mathbf{y},t)\cdot\mathbf{J}(\mathbf{x}|\mathbf{y})\,d\Gamma_\mathbf{y}+\frac{1}{\eta_s}\left(\frac{\lambda_s}{\Delta t}+1\right)\int_{\Gamma_i(t)}\mathbf{t}_s(\mathbf{y},t)\cdot\mathbf{J}(\mathbf{x}|\mathbf{y})\,d\Gamma_\mathbf{y}\\&-\int_{\Gamma_i(t)}\mathbf{n}(\mathbf{y},t)\cdot\mathbf{u}_i(\mathbf{y},t)\cdot\mathbf{K}(\mathbf{x}|\mathbf{y})\,d\Gamma_\mathbf{y}\\&=\frac{\lambda_s}{\eta_s\Delta t}\int_{\Gamma_i(t)}\mathbf{t}_s(\mathbf{y},t-\Delta t)\cdot\mathbf{J}(\mathbf{x}|\mathbf{y})\,d\Gamma_\mathbf{y}+\int_{\Gamma_c}\mathbf{n}(\mathbf{y})\cdot\mathbf{u}_c(\mathbf{y})\cdot\mathbf{K}(\mathbf{x}|\mathbf{y})\,d\Gamma_\mathbf{y}+\begin{cases}\mathbf{u}_s(\mathbf{y},t), & \mathbf{x}\in\Omega_s(t)\\ c_s(\mathbf{x},t)\mathbf{u}_s(\mathbf{y},t), & \mathbf{x}\in\Gamma_c\\ c_s(\mathbf{x},t)\mathbf{u}_i(\mathbf{y},t), & \mathbf{x}\in\Gamma_i(t)\\ \mathbf{0} & \mathbf{x}\in\Omega_d(t)\end{cases}\end{aligned} \tag{29}$$

whereas Equation (26) is rewritten as

$$\begin{aligned}&\frac{1}{\eta_d}\left(\frac{\lambda_d}{\Delta t}+1\right)\int_{\Gamma_i(t)}\mathbf{t}_d(\mathbf{y},t)\cdot\mathbf{J}(\mathbf{x}|\mathbf{y})\,d\Gamma_\mathbf{y}-\int_{\Gamma_i(t)}\mathbf{n}(\mathbf{y},t)\cdot\mathbf{u}_i(\mathbf{y},t)\cdot\mathbf{K}(\mathbf{x}|\mathbf{y})\,d\Gamma_\mathbf{y}\\&=\frac{\lambda_d}{\eta_d\Delta t}\int_{\Gamma_i(t)}\mathbf{t}_d(\mathbf{y},t-\Delta t)\cdot\mathbf{J}(\mathbf{x}|\mathbf{y})\,d\Gamma_\mathbf{y}+\begin{cases}\mathbf{0} & \mathbf{x}\in\Omega_s(t)\cup\Gamma_c\\ c_d(\mathbf{x},t)\mathbf{u}_d(\mathbf{y},t), & \mathbf{x}\in\Gamma_i(t)\\ \mathbf{u}_d(\mathbf{y},t), & \mathbf{x}\in\Omega_d(t)\end{cases}\end{aligned} \tag{30}$$

The abbreviation $\mathbf{T}_s(\mathbf{x},t)=\lambda_s\,[\partial\mathbf{t}_s(\mathbf{x},t)/\partial t]+\mathbf{t}_s(\mathbf{x},t)$, $\mathbf{x}\in\Gamma_c$, has been introduced. This term can be considered as a generalized traction and is determined as an unknown without having to resort to a finite difference of the time derivative.

Before manipulating further Equations (29) and (30), it is convenient to introduce the following abbreviations:

$$\alpha_s\equiv\left(\frac{\lambda_s}{\Delta t}+1\right)^{-1},\qquad\alpha_d\equiv\left(\frac{\lambda_d}{\Delta t}+1\right)^{-1},\qquad R_\eta\equiv\frac{\eta_d}{\eta_s} \tag{31}$$

where R_η is the drop-to-suspending fluid viscosity ratio. The multiplication of Equation (29) by α_s and Equation (30) by $R_\eta\alpha_d$, the addition of the resulting equations, and the use of boundary conditions (11) lead to

$$\int_{\Gamma_i(t)} \left\{ (R_\eta \alpha_d - \alpha_s)\mathbf{n}(\mathbf{y}, t)\cdot\mathbf{u}_i(\mathbf{y}, t)\cdot\mathbf{K}(\mathbf{x}|\mathbf{y}) + \frac{\gamma}{\eta_s}\kappa(\mathbf{y}, t)\mathbf{n}(\mathbf{y}, t)\cdot\mathbf{J}(\mathbf{x}|\mathbf{y}) \right\} d\Gamma_y$$
$$-\frac{\alpha_s}{\eta_s}\int_{\Gamma_c} [\mathbf{T}_s(\mathbf{y}, t)\cdot\mathbf{J}(\mathbf{x}|\mathbf{y})]\, d\Gamma_y = (R_\eta \alpha_d + \alpha_s)c_d(\mathbf{x}, t)\mathbf{u}_d(\mathbf{x}, t)$$
$$-\frac{1}{\eta_s \Delta t}\int_{\Gamma_i(t)} \{[(\lambda_s\alpha_s - \lambda_d\alpha_d)\mathbf{t}_d(\mathbf{y}, t-\Delta t)$$
$$-\lambda_s\alpha_s\gamma\kappa(\mathbf{y}, t-\Delta t)\mathbf{n}(\mathbf{y}, t-\Delta t)]\cdot\mathbf{J}(\mathbf{x}|\mathbf{y})\}\, d\Gamma_y$$
$$-\alpha_s\int_{\Gamma_c} [\mathbf{n}(\mathbf{y})\cdot\mathbf{u}_c(\mathbf{y})\cdot\mathbf{K}(\mathbf{x}|\mathbf{y})]\, d\Gamma_y, \quad \mathbf{x}\in\Gamma_i(t) \tag{32}$$

Another integral equation is also needed, which governs the value of the velocity and traction on the walls of the channel. It can be derived similarly to read

$$\frac{1}{\eta_s}\int_{\Gamma_c} \mathbf{T}_s(\mathbf{y}, t)\cdot\mathbf{J}(\mathbf{x}|\mathbf{y})\, d\Gamma_y + \frac{R_\eta\alpha_d - \alpha_s}{\alpha_s}\int_{\Gamma_i(t)} [\mathbf{n}(\mathbf{y}, t)\cdot\mathbf{u}_i(\mathbf{y}, t)\cdot\mathbf{K}(\mathbf{x}|\mathbf{y})]\, d\Gamma_y$$
$$= c_s(\mathbf{x}, t)\mathbf{u}_c(\mathbf{x}) + \int_{\Gamma_c} [\mathbf{n}(\mathbf{y})\cdot\mathbf{u}_c(\mathbf{y})\cdot\mathbf{K}(\mathbf{x}|\mathbf{y})]\, d\Gamma_y$$
$$-\frac{1}{\eta_s\alpha_s}\int_{\Gamma_i(t)} \left[\gamma\kappa(\mathbf{y}, t)\mathbf{n}(\mathbf{y}, t) - \frac{\lambda_s\alpha_s - \lambda_d\alpha_d}{\Delta t}\mathbf{t}_d(\mathbf{y}, t-\Delta t) \right]\cdot\mathbf{J}(\mathbf{x}|\mathbf{y})\, d\Gamma_y, \quad \mathbf{x}\in\Gamma_c \tag{33}$$

where the boundary condition (9) for the velocity along Γ_c has been used. The normal vector on Γ_c is independent of time, which leads to the time derivative of the traction (instead of the stress) in the integrals along the channel. As the velocity on Γ_c is fully prescribed only the traction needs to be determined at that boundary.

Equations (32) and (33) represent two coupled equations for the velocity at the interface, $\mathbf{u}_i(\mathbf{x}\in\Gamma_i, t)$, and the generalized traction at the channel, $\mathbf{T}_s(\mathbf{x}\in\Gamma_c, t)$. Also, following the determination of these unknowns, the flow field off the interface and cavity wall can be calculated using the appropriate equations in regions $\Omega_d(t)$ and $\Omega_s(t)$.

4.3. Numerical implementation

The numerical solutions of Equations (32) and (33) are obtained in a similar way as those of the Newtonian problem [55]. The equations are discretized into a finite sum of contributing terms over the boundaries. In this study, the simplest form of the BEM is adopted, and the velocity and traction are assumed to be constant over each boundary element. The resulting algebraic system is solved using the LU factorization method. For the present problem, the duct bounding the surrounding (ambient) fluid is discretized into triangular elements along with the interface between drop and ambient fluid. The geometrical flow model is illustrated schematically in Figure 1. The flow of the suspending fluid is induced by the action of a driving pressure gradient of the Poiseuille type, although other types of flow are also used (see below).

Consider now the application of the integral equations (32) and (33) for a point on the boundary, i.e., for $\mathbf{x}\in\Gamma_c\cup\Gamma_i(t)$. The flow field at any interior point $\mathbf{x}\in\Omega(t)$ is obtained once the variables at the boundary are known. Since the velocity is fully prescribed on the stationary boundary, Γ_c, only the traction (or stress) will be determined there. The time derivative in Equation (10) is approximated by an explicit Eulerian finite difference scheme, with higher-order terms in the time increment, Δt, being neglected. Once the flow field is determined at each time step, t, the position of the interface is updated. The evolution of $\Gamma_i(t)$ is dictated by Equation (10). The integrals in Equation (10) are discretized into a finite sum of contributing terms over the boundaries. In this work, the boundary elements are assumed to be geometrically linear so that the velocity and traction are constant over each element. The use of higher-order elements is possible, but is not crucial given the mesh refinement and remeshing capabilities involved in the current procedure. The traction is constant over flat linear element, and is multiply valued at a corner node if higher-order elements are used. Although this problem is efficiently circumvented in two-dimensional problems [22], it remains a major open issue for a complex three-dimensional geometry. In two dimensions, the traction is assumed to be double valued at every node of a curved boundary. Another advantage of the constant boundary element is that the value of $c(\mathbf{x}, t)$ is always and everywhere equal to $\frac{1}{2}$. In addition, the normal vector to each element is determined exactly.

4.4. Adaptive meshing

Khayat and Marek [4] gave a detailed account of the adaptive meshing used for an interface or free surface. The treatment follows closely the method proposed by Nambiar *et al*. [56], who adopted two-dimensional mesh refinement for finite element problems. Only a summary of the method will be given here. A simple algorithm is proposed for the adaptive refinement of the (two-dimensional) triangular mesh of the evolving interface. Initially ($t<0$), the drop is assumed to occupy a three-dimensional region, $\Omega_d(t<0)$ bounded by the interface $\Gamma_i(t<0)$. As the drop deforms, some or all of the elements grow in size; depending on the ambient flow, the element may grow or decrease in size.

When the interface deforms, mesh refinement is carried out by sub-dividing the elements that are too distorted. Generally, the criteria for sub-division are based on the element area and the length of the edges. However, it turns out that the length of the longest edge is a reliable criterion by itself. In this case, at each time step of the flow, a list of elements is established, with the length of the longest edge greater than an imposed tolerance, $D_{\max}$. The list is sorted in the order of increasing length of the longest edges of each element. In order to avoid generating mesh incompatibilities or elements with poor aspect ratio during refinement, larger elements are subdivided first. The sub-division starts from the last (i.e. the longest edge) element in the list, and is continued recursively until the list is empty. The sub-division is carried out by bisecting the largest of the edges of the element in the list.

Two distinct cases of element sub-division arise. In the first case, the edge that is being sub-divided is on the boundary of the domain, and in the second case the edge is inside the domain. To prevent the creation of any non-conforming elements in the second case, the element that shares the common longest edge is also bisected along with the first element. The creation of four elements in such a manner is carried out only when the bisected edge is the

longest edge of both elements. If this condition is not met, the second element is added to the end of the element list, which contains the distorted elements so that the second element is now the current element for sub-division and the process is repeated. Again, the element selected for sub-division will have an edge that is the longest among the edges of the elements in the list.

In order to facilitate the search process for the second element and the longest edge of elements, the input data are initially processed to create three data structures, one structure each for nodes, triangles, and edges. A node is defined by its x, y, and z co-ordinate. The properties selected for a triangle are its three nodes, A, B, and C; its three edges, AB, BC, and CA; and its area. The above information is structured such that the node numbers are ordered in a counterclockwise direction for each element and edge AB is the longest edge of each element. The properties of an edge are its two end nodes, its two neighboring triangles, and the length of the edge.

The major advantage of dividing only the longest edge in a triangle is that the smallest angle in the original mesh is not further sub-divided. Let, for example, C and A be the largest and smallest angles respectively. If the (largest) angle C is greater than 90°, none of the newly created angles can be smaller than the original (smallest) angle A. If C is equal to 90°, the smallest angle A is duplicated as D. If, however, C is smaller than 90°, the newly created angle D is slightly smaller than A. Further, if an angle A is smaller that 60°, it will never be bisected using this algorithm. Rosenberg and Stenger [57] have shown that the smallest angle that can be created in any subsequent mesh produced by the above method is bounded by half the minimum angle present in the initial mesh. Thus, the aspect ratio of the triangles in the mesh remains in an acceptable and known range.

The first step in the solution is to create the data file containing the description of the problem domain, boundary conditions, loading, and initial mesh. The initial mesh is first examined to check for initially distorted elements. This mesh comes from a computer-aided design (CAD) system, such as PATRAN, PROENGINEER, or I-DEAS. The initial mesh is then refined by the adaptive remeshing scheme described above. The refined mesh is then submitted to the BEM solver. In practice it is found that the quality of the initial mesh is adequate, and initial refinement is generally not necessary.

4.5. Determination of local curvature

The value of the curvature at a particular location (node) on the free surface is needed if surface tension is to be accounted for. The curvature is obviously related to the divergence of the normal vector, $\mathbf{n}(\mathbf{x}, t)$, at the location in question. Thus, the determination of the curvature is based on the estimation of the derivative of the normal vector components in the three directions. For this, it is convenient to define local co-ordinates spanned by the plane tangent to the surface at the local point and the normal to the plane [4].

Consider now the curvature at an element (centroid) of the discretized surface. Generally, each node of the triangle belongs to an arbitrary number of elements, and the normal at the node is not uniquely defined. The normal vector is then taken as the area average of the normal vectors to the elements to which the node belongs. The normal vector anywhere to the element is expanded in terms of suitably introduced interpolation functions, which allow the determination of the curvature—$\nabla\cdot\mathbf{n}/2$. This procedure was validated by computing the

curvature for simple surfaces, which were discretized in triangular flat elements. Two cases were treated, namely, the case of a spherical shell of radius equal to 1, and the case of a parabolic surface [4].

5. NUMERICAL ASSESSMENT AND RESULTS

The calculations focus on the deformation of a drop in simple shear and duct flows. Both fluids are assumed to be in a state of creeping motion as inertia effects are negligible for most polymeric liquids. Since the rate of drop deformation is slow, it is reasonable to assume that normal stress effects (which lead to the well-known Weissenberg rod-climbing phenomenon) are small enough for the fluid to obey a linear viscoelastic constitutive equation. The results are restricted to fluids that obey Maxwell's constitutive model.

The validation of the formulation and solution procedure is first demonstrated for simple two-phase flow configuration for which analytical solutions exist. Both Newtonian and viscoelastic systems will be considered. The influence of mesh size and refinement will then be assessed for simple shear flow. The general performance of the basic three-dimensional BEM code was previously evaluated through comparison with the FEM, using the commercial package POLYFLOW™ for one-phase confined flow [1] (see also References [5,29,30] for the two-dimensional case). The accuracy for the two-dimensional code was assessed by comparing the velocity in the axial and transverse directions for the flow inside a (plane) channel with sudden contraction. Excellent agreement between the BEM and FEM data was obtained [5]. The performance of the three-dimensional code was assessed for simple cavity flow; good agreement was also achieved [8].

5.1. Comparison between analytical and numerical solutions

Consider the two-phase azimuthal flow of incompressible viscoelastic fluids around a spherical object as shown in Figure 2. There is an analogy between this problem and the deformation of the drop inside a confined medium as illustrated in the notations in the figure. The sphere plays the role of the confining cavity in Figure 1. The fluid in the immediate vicinity to the sphere occupies the region $r \in [R_c, R_i]$ and replaces the suspending fluid, where R_c is the radius of the rotating sphere and R_i is the location of the interface between the two fluids. The second fluid occupies the region bounded by the interface and extends to infinity; it replaces the drop. Let $R_c = 1$ cm and $R_i = 2$ cm. The sphere is assumed to start rotating from rest at an angular speed $\Omega = t$ rad s^{-1}, entraining with it the two fluids in circular motion. This time-dependent rotation will induce a transient behavior in the two fluid regions, making the unsteady terms in the governing equations non-vanishing. While the interface can be considered as fixed, it has been assumed to rotate with the fluids similarly to the case of a deforming drop. In this case, Equation (10) still applies. The aim of this section is to first determine analytically the azimuthal velocity and traction components at the interface, and then compare them with the numerical solution. This situation is comparable with the problem of drop deformation, where the velocity and traction are calculated at the interface.

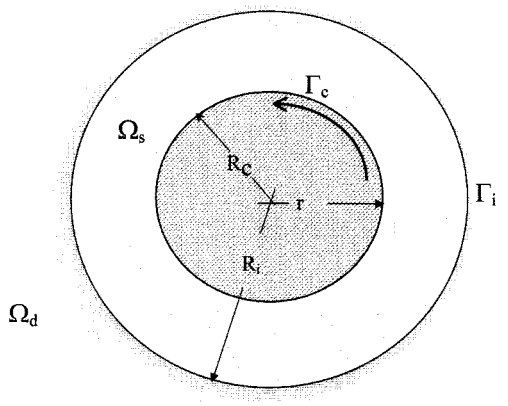

Figure 2. Spherical flow of two-phase viscoelastic system. The analogy with the system in Figure 1 is established by noting that, in this case, region $\Omega_s = [R_c, R_i]$ and region $\Omega_d = [R_i, \infty)$.

Consider now the general flow field in the two regions: $\Omega_s \equiv \{r | R_c < r \leq R_i\}$ and $\Omega_d \equiv \{r | R_i \leq r < \infty\}$. Although the analytical solution can be obtained for Oldroyd-B fluids, the comparison will be limited to Maxwell fluids. In this case, the fluids in question are polymer melts and not solutions: $\eta_\alpha^{(s)} = 0$ and $\eta_\alpha = \eta_\alpha^{(p)}$. The only non-vanishing velocity and stress components are the azimuthal components. The general expression for the velocity is given by

$$u_\phi(r, \theta, t) = \begin{cases} \left[\dfrac{G_s(t)}{3\eta_s r^2} + H_s(t) r\right] \sin\theta, & r \in [R_c, R_i] \\ \dfrac{G_d(t)}{3\eta_d r^2} \sin\theta, & r \in [R_i, \infty) \end{cases} \tag{34}$$

and the expression for the shear stress is of the form

$$\tau_{r\phi}(r, \theta, t) = \begin{cases} \dfrac{F_s(t)}{r^3} \sin\theta, & r \in [R_c, R_i] \\ \dfrac{F_d(t)}{r^3} \sin\theta, & r \in [R_i, \infty) \end{cases} \tag{35}$$

where $F_\alpha(t)$, $G_\alpha(t)$ and $H_\alpha(t)$ are general time-dependent functions. Note that the solutions above satisfy the conservation equations (5) and (6). In addition, the stress must satisfy the constitutive equation (7), leading to

$$\lambda_\alpha \frac{\mathrm{d}F_\alpha(t)}{\mathrm{d}t} + F_\alpha(t) = -G_\alpha(t) \tag{36}$$

Note that interfacial tension effects are not implicated in the present problem as no normal forces are involved. Conditions (11) for the continuity of the velocity and stress at the interface $r = R_\mathrm{i}$, as well as the boundary condition (9) at the cylinder give three additional equations to Equation (36) to determine the time-dependent integration functions. After some manipulation, the time-dependent expressions for the velocity and stress at the interface are given by

$$u_\phi(R_i, \theta, t) = \frac{R_r \lambda_\mathrm{d}}{\beta^2}\left[\beta - \frac{1}{\lambda_\mathrm{d}} + \beta t + \left(\frac{1}{\lambda_\mathrm{d}} - \beta\right)\mathrm{e}^{-\beta t}\right]\sin\theta \tag{37}$$

$$t_\phi(R_\mathrm{i}, \theta, t) = \frac{3R_r\eta_\mathrm{d}}{R_\mathrm{i}[R_\eta\lambda_\mathrm{s}(R_r^2 - 1) - \lambda_\mathrm{d}]\beta^2}(\beta t - 1 + \mathrm{e}^{-\beta t})\sin\theta \tag{38}$$

where $R_r = R_\mathrm{i}/R_\mathrm{c}$ is the aspect ratio, and $\beta = [R_\eta(R_r^2 - 1) - 1][\lambda_\mathrm{s}R_\eta(R_r^2 - 1) - \lambda_\mathrm{d}]$.

Consider the case when the fluids in the regions Ω_s and Ω_d have relaxation time $\lambda_\mathrm{s} = 0.5$ s and $\lambda_\mathrm{d} = 1.5$ s respectively. The viscosity ratio is taken equal to 3. The evolution of the velocity at the interface is shown in Figure 3. The figure displays the analytical solution based on Equation (37) and the numerical results based on six time increments ranging from 0.002 to 0.5 s. The mesh size is kept the same for all cases; 200 elements are taken for the sphere and 200 elements for the interface ($r = R_\mathrm{i}$). There is good agreement generally, even for the coarsest time step used. The case of a Newtonian system is also included. The numerical solution is carried out with $\Delta t = 0.1$ s. Similar convergence rates and agreement are obtained between analytical and numerical solutions for the azimuthal traction. The results are shown in Figure 4. Further assessment of the accuracy will be made next when the deformation of a three-dimensional drop inside a channel is considered.

5.2. Deformation of a drop in simple shear flow and further assessment of accuracy

The present formulation and computer implementation are further assessed for the problem of drop deformation in simple shear flow. Aside from a drop of properties similar to those of the suspending fluid, the numerical solution cannot be compared with an analytical solution. However, the convergence and accuracy of the method can still be assessed by varying the time increment and/or mesh size. The error is reflected in the volume change of the drop as it deforms with time. The effect of time increment for a fixed mesh size has been extensively examined for two-dimensional drop deformation problems [29–34]. It is usually found that, for a given time increment, the error increases with time. The error is, however, controlled to any degree of accuracy by decreasing the time increment. So the effect of the time increment will not be explored here as the effect of mesh size is of more relevance to the present (three-dimensional) formulation.

Consider the evolution of the drop as it deforms under the action of ambient simple shear flow. The shear flow is in the (y, z) plane, with the velocity in the z-direction and given by $w = y/2$ as shown in Figure 5. The figure shows a typical deformation stage with the mesh used for the drop interface. Both suspending fluid and drop are Newtonian ($\lambda_\mathrm{s} = \lambda_\mathrm{d} = 0$ s). The drop

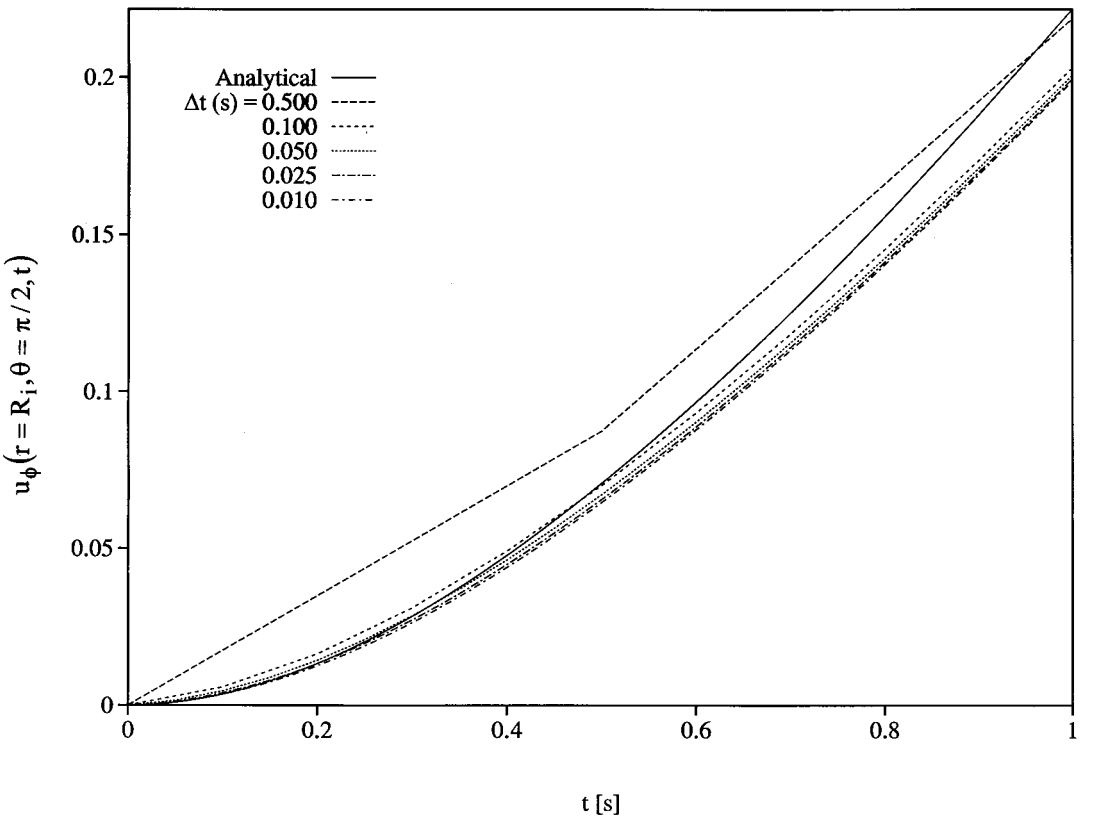

Figure 3. Evolution of velocity at the spherical interface. Comparison between analytical and numerical solution for $0.025 \leq \Delta t$ (s) ≤ 0.5.

and suspending fluid viscosities are the same ($R_\eta = 1$). The drop is initially spherical with initial radius equal to 0.2 (unit length). Figures 6–9 display the evolution of the drop as it deforms with time.

The initial configuration is shown in Figure 6 in the (x, y, z) space (Figure 6(a)), with projections in the (x, y) plane (Figure 6(b)), the (y, z) plane (Figure 6(c)) and the (x, z) plane (Figure 6(d)). Obviously, in this case the four perspectives give the same information. Figure 7 shows the deformation of the drop after 2 s. The overall extension is obvious in the (x, y, z) space (Figure 7(a)), from the (y, z) plane (Figure 7(c)), and the elliptical shape in the (x, z) plane (Figure 7(d)). At 8 s, there is pronounced thinning as shown in the (y, z) plane of Figure 8(c). The corresponding flattening is also obvious in the (x, z) plane (Figure 8(d)). Note that the symmetry is preserved overall. Finally, Figure 9 displays the deformation of the drop after 10 s. This figure shows a similar but a more enhanced deformation than in Figure 8. There is also a slight loss of symmetry due to numerical error (see Figure 9(c)).

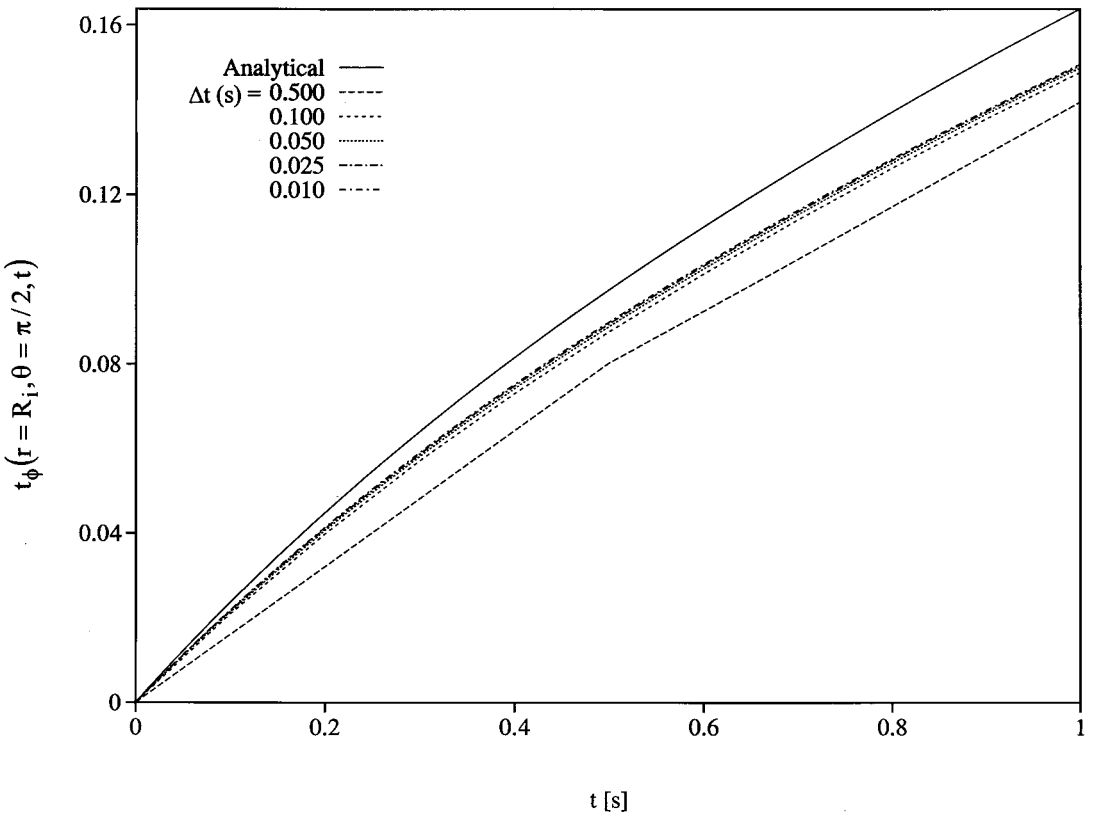

Figure 4. Evolution of radial traction at the spherical interface. Comparison between analytical and numerical solution for $0.025 \leq \Delta t$ (s) ≤ 0.5.

The influence of mesh size on the evolution of the error is displayed in Figure 10. As mentioned earlier, the mesh size is dictated by the length of the longest element edge, $D_{\max}$. Thus, when $D_{\max}$ is small, the surface elements tend to sub-divide more often than when $D_{\max}$ is large. The figure shows the error for $D_{\max} \in [0.15, \infty)$ (cm) for a sphere of initial radius equal to 0.2 cm, indicating that the error growth is effectively controlled by $D_{\max}$. Note that $D_{\max}$ is infinite (larger than 0.4 cm in the current problem), and no element sub-division occurs in this case. It is found from the figure that, for a given $D_{\max}$, the error tends to generally initially increase sharply with time, but seems to somewhat level out thereafter. The initial period of error growth corresponds to a period when no element sub-division has taken place yet. At this stage, the value of $D_{\max}$ has no influence as, although the elements at the interface continue to deform, the criterion for element sub-division would not yet be satisfied. Once the element size reaches $D_{\max}$, the process of element sub-division begins, and the sharp error growth starts to decrease. This seems to be typically the case for the curves corresponding to $D_{\max} \in [0.3, 0.2]$

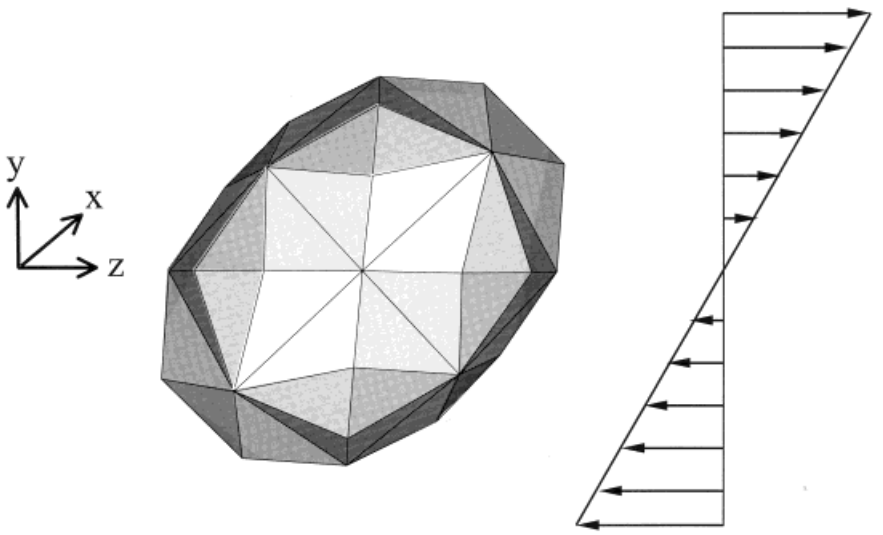

Figure 5. Typical deformation of a three-dimensional drop subject to ambient shear flow. The figure shows the type of mesh used and co-ordinate systems.

(cm), as these curves display a slight overshoot in the error. Note that the curve $D_{\max} = 0.15$ cm does not display an overshoot. The non-monotonic and sudden change in error behavior is closely correlated with the change in the number of elements.

Figure 11 displays the evolution of the number of elements at the drop/matrix interface as the drop deforms with time for the same range of $D_{\max}$ values as before. In general, the number of elements increases with time, except for the crudest mesh ($D_{\max} = \infty$), where the number of elements remains unchanged (72 elements). Obviously, given the discreteness of the process of element sub-division, the evolution of element number occurs stepwise. Thus, one expects the error to decrease with deformation. The overall correlation between the number of elements in Figure 11 and the relative error in Figure 10 is easily inferred from the two figures. In particular, the onset of the overshoot in relative error coincides with a sudden increase in the number of elements, as is typically indicated by the curves corresponding to $D_{\max} = 0.20$ cm.

5.3. Deformation of a drop in duct flow and influence of fluid elasticity

The influence of fluid properties on drop deformation is now examined for a drop deforming in a confined medium. The influences of viscosity ratio, interfacial tension, and drop elasticity are explored. So, consider the evolution of a drop as it deforms under the action of the ambient flow in a cylindrical (straight) duct. The situation is again typically illustrated in Figure 1. The cylindrical duct is discretized into 362 triangular elements. Obviously, while the number of duct elements remains constant, that of the drop interface grows with drop

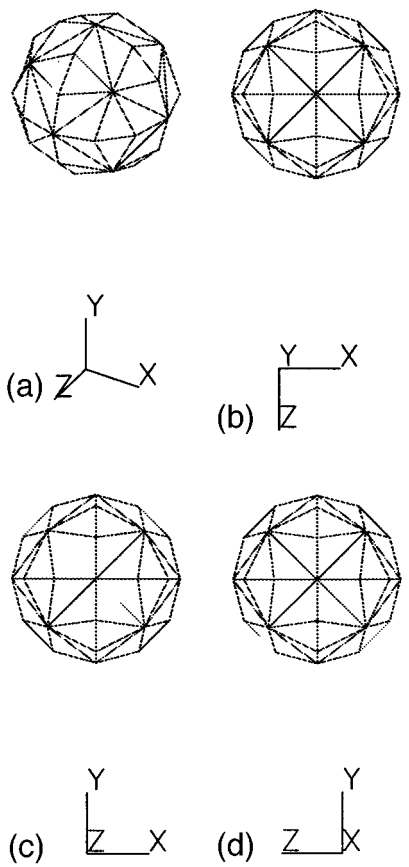

Figure 6. Deformation of a drop in simple shear flow ($R_\eta = 1$). Both suspending fluid and drop are Newtonian ($\lambda_s = \lambda_d = 0$ s). Figure shows initial spherical drop in the (x, y, z) space (a), with projections in the (x, y) plane (b), the (y, z) plane (c), and the (x, z) plane (d).

deformation. The interface is discretized initially into 72 elements. This number of elements turned out to be sufficient as it leads to a reasonable (order of one) duct/drop element ratio. It is found that it is the element ratio, and not so much the actual number of elements that influences the solution accuracy.

Figure 12 shows the boundary element mesh at a typical deformation stage of an initially spherical drop inside a cylindrical duct. As expected in duct flow, the drop front tends to elongate, while the drop tale tends to flatten out. Both drop and suspending fluid are assumed to be Newtonian ($\lambda_s = \lambda_d = 0$ s). The duct has a length-to-radius ratio equal to 16. The z-direction is taken along the cylinder axis, originating at the beginning of the cylinder lying in the (x, y) plane. The deformation of the drop is induced by the ambient flow in the duct, which corresponds to Poiseuille flow, which is imposed at the two ends of the duct. Thus, the

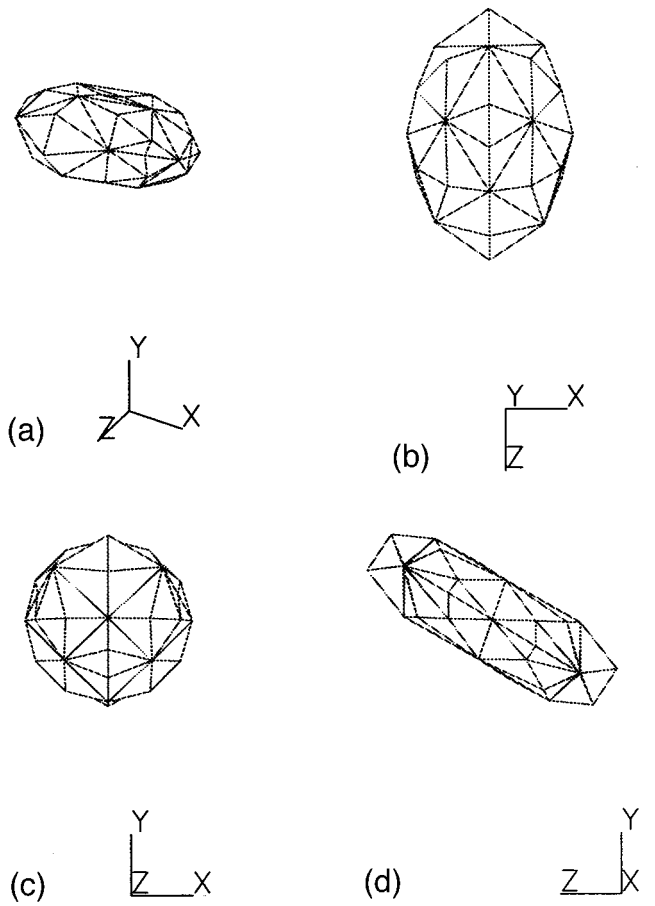

Figure 7. Deformation of the drop initially shown in Figure 6 after 2 s. Shown is the deformed drop in the (x, y, z) space (a), circular projections in the (x, y) plane (b), elongated drop in the (y, z) plane (c), and elliptical shape in the (x, z) plane (d).

drop is assumed at all times to be located away from the ends of the duct for Poiseuille conditions to apply there.

The influence of fluid properties is assessed by monitoring the evolution of the deformation with time, which is defined as the relative change in the surface area, $S(t)$, of the drop, namely $(S - S_0)/S_0$, where S_0 is the initial surface area of the drop. Given the high deformation induced by the ambient flow an ellipsoidal drop was assumed, of minor and major axes equal to 0.4 and 1 cm respectively. Recall that the length of the duct is 16 cm and its diameter is 2 cm The drop is initially centered at $z = 5$ cm on the axis of the duct. In what follows, the influence of viscosity ratio and interfacial tension will be examined next. In all calculations,

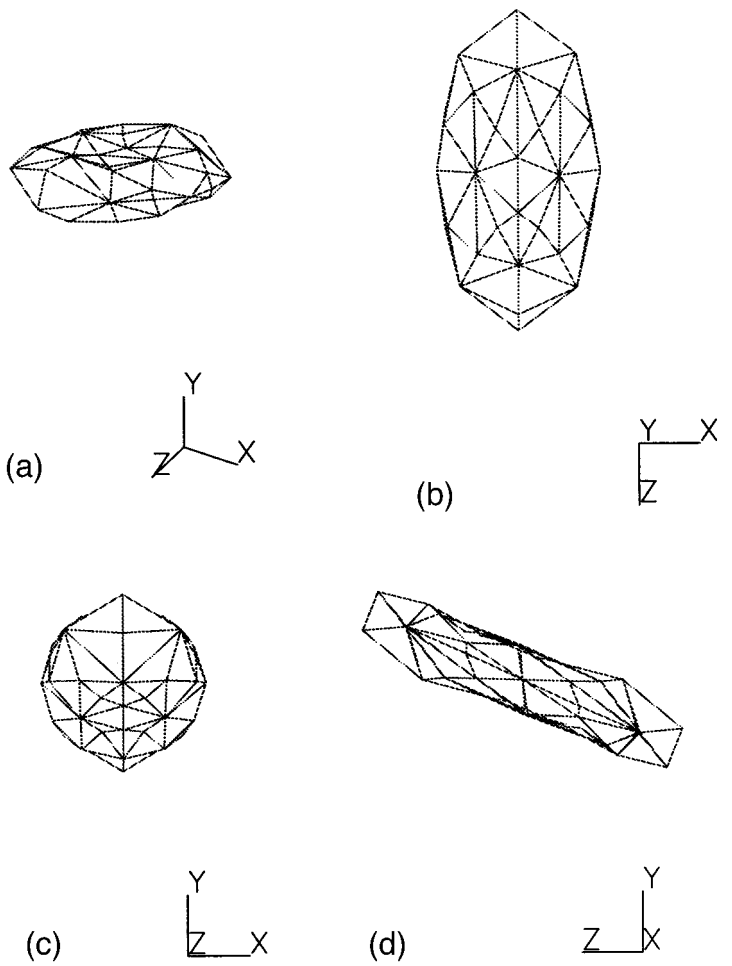

Figure 8. Deformation of the drop initially shown in Figure 6 after 8 s. Shown is the deformed drop in the (x, y, z) space (a), circular projections in the (x, y) plane (b), pronounced thinning in the (y, z) plane (c), and flattening in the (x, z) plane (d). Note that symmetry is preserved overall.

$D_{\max} = 0.6$ cm and $\Delta t = 0.01$ s. Consider first the influence of the viscosity ratio, R_η. Figure 13 displays the deformation of a drop with interfacial tension coefficient $\gamma = 1$ dyn cm^{-1} and $R_\eta \in [2, 10]$. The deformation is monitored over a period of 0.8 s. For any viscosity ratio, the deformation rate is relatively low initially. As the drop deforms further, the deformation increases, but ultimately slows down again in the later stages. This is reflected by the relative flattening of the curves in the figure. It is clear from the figure that deformation is lower as R_η increases. Thus, as expected, drop viscosity tends to inhibit deformation. This behavior was also confirmed for viscoelastic systems.

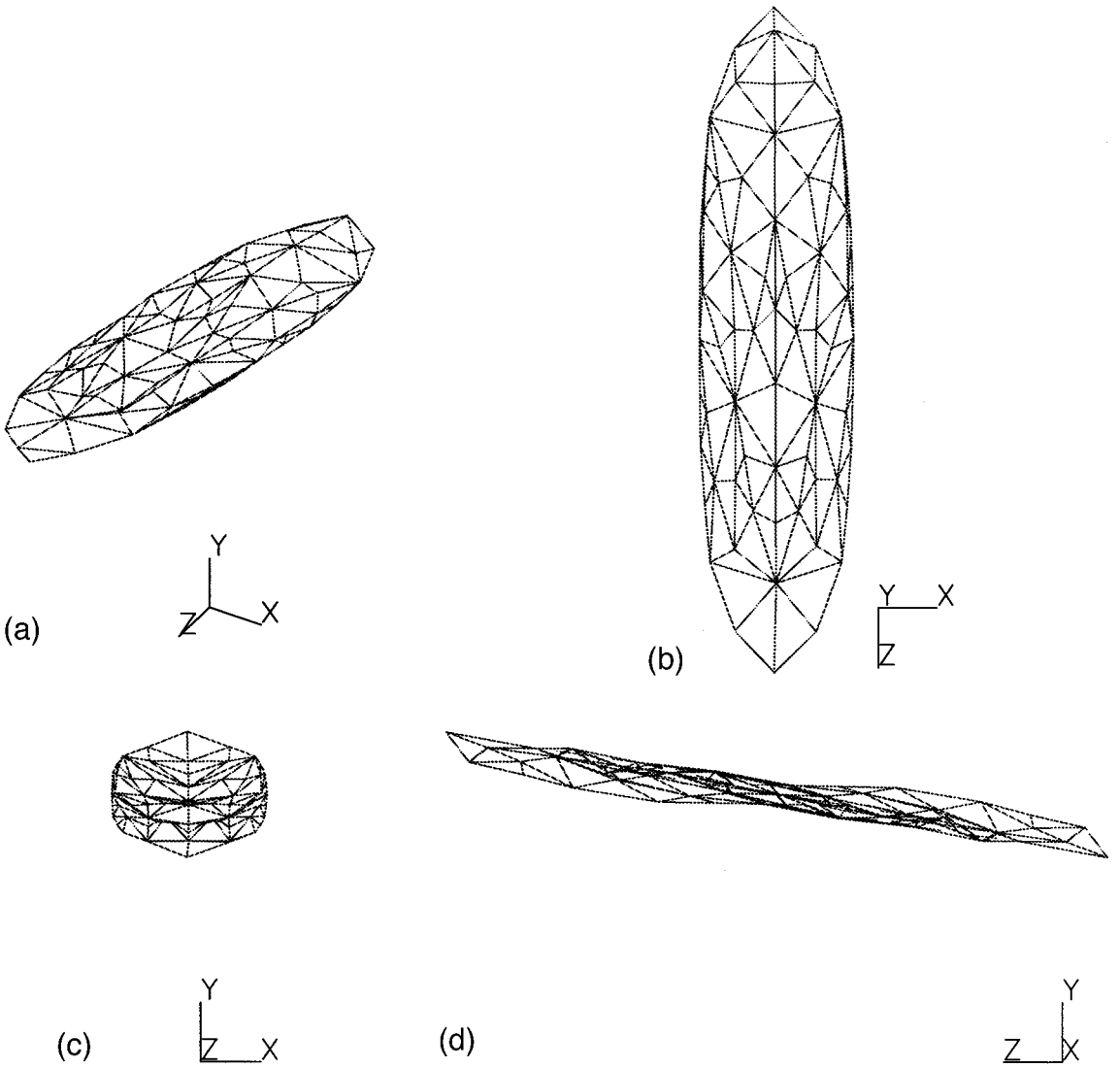

Figure 9. Deformation of the drop initially shown in Figure 6 after 10 s. What is shown is a similar but a more enhanced deformation than in Figure 8. There is also a slight loss of symmetry due to numerical error (see (c)).

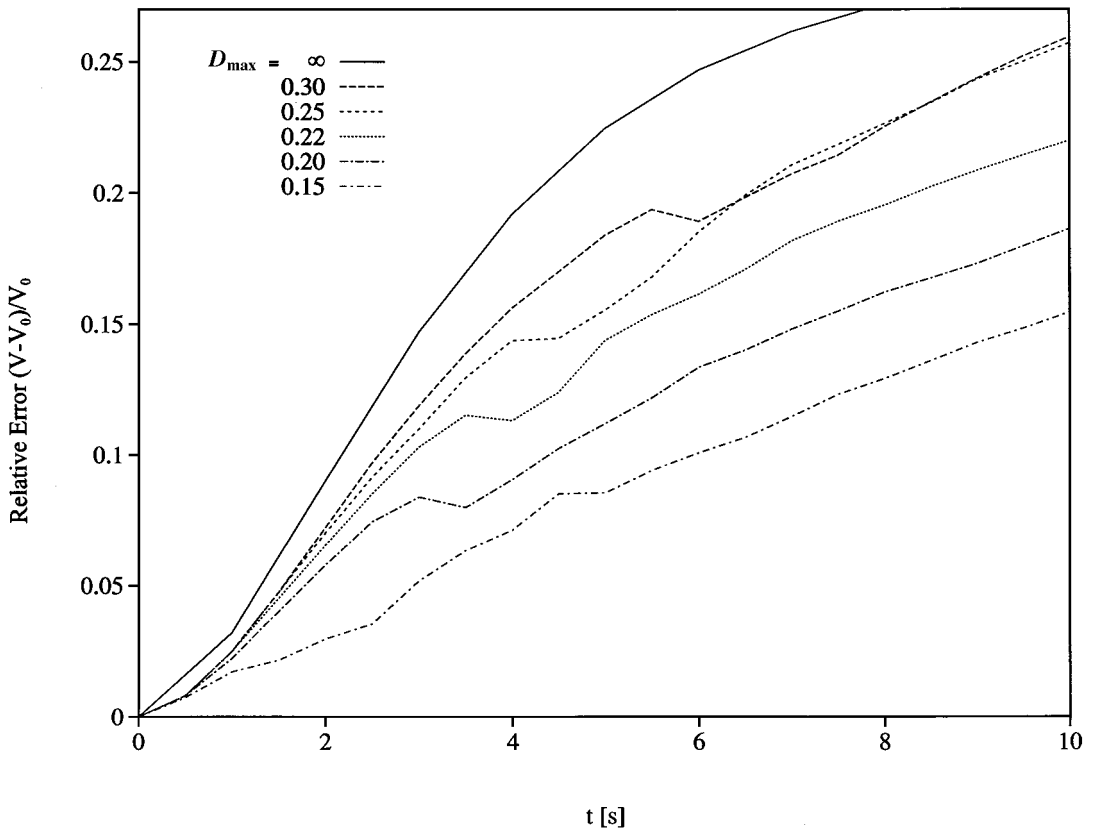

Figure 10. Influence of mesh refinement on the evolution of the relative error for a drop as in Figure 5. The error is measured as the relative volume change $(V - V_0)/V_0$ of a drop deforming in shear flow. The error is plotted as function of time for $D_{max} \in [0.15, \infty)$.

The influence of interfacial tension is displayed in Figure 14 for $\gamma \in [0, 4]$ (dyn cm^{-1}) and $R_\eta = 5$. Again, both drop and suspending fluid are Newtonian ($\lambda_d = 0$ and $\lambda_s = 0$). The deformation evolves overall very similar to that in Figure 13. The figure indicates that interfacial tension prohibits deformation, similarly, to drop viscosity. This is particularly obvious from the curve corresponding to $\gamma = 4$ dyn cm^{-1}. In this case, the drop is observed to simply translate inside the duct without deforming in the early stages. It is only after 0.15 s that a deformation is perceptible.

Finally, the influence of fluid elasticity is examined for the same ellipsoidal drop. In this case, the drop is taken to be elastic ($\lambda_d \neq 0$), and the ambient flow is assumed to be Newtonian ($\lambda_s = 0$). The relaxation times examined range from $\lambda_d = 0$ s for a Newtonian drop to 0.3 s. The viscosity ratio is fixed at $R_\eta = 3$. The interfacial tension coefficient is also fixed $\gamma = 1$ dyn cm^{-1}.

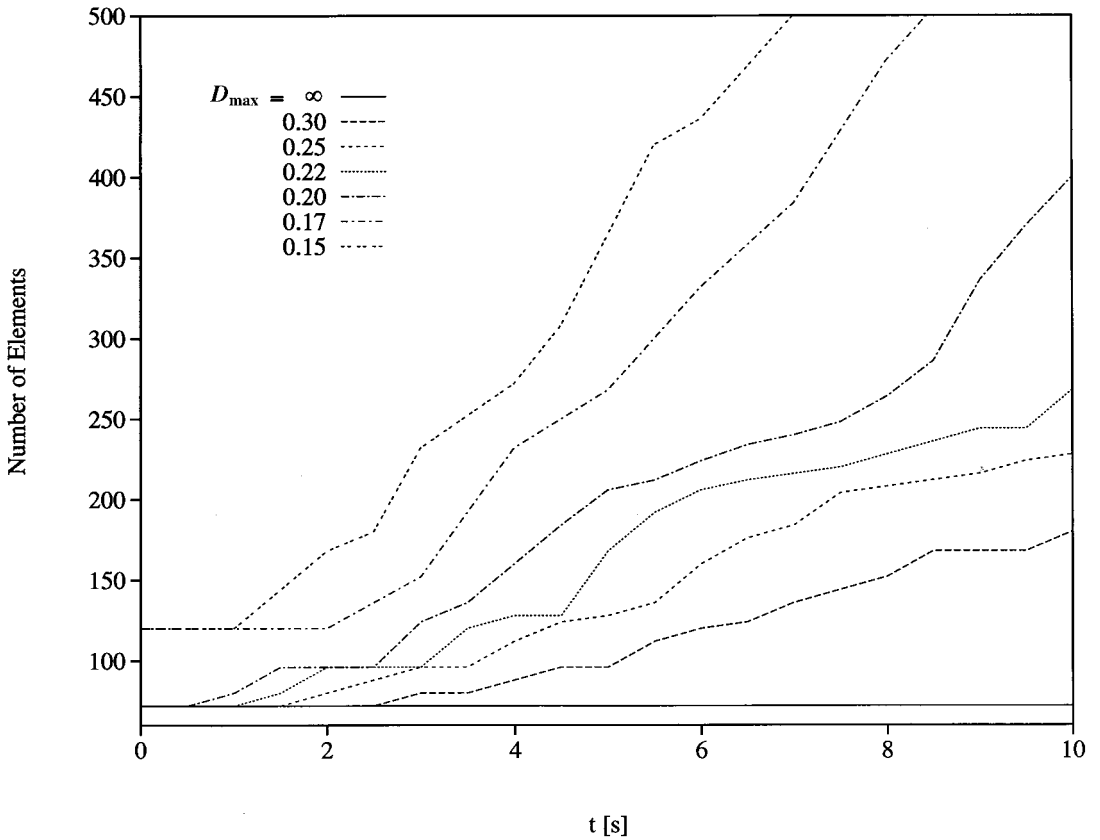

Figure 11. Evolution of number of elements at the drop interface in simple shear flow as function of time for $D_{max} \in [0.15, \infty)$.

Consider the evolution of the drop as it deforms under the action of the ambient flow in the circular duct as above. The influence of the relaxation time, λ_d, of the drop is shown in Figure 15. The figure displays the evolution of the deformation of a drop with $\lambda_d \in [0, 0.3]$ (s) in a Newtonian suspending fluid ($\lambda_s = 0$ s). The case of a Newtonian drop moving in a Newtonian matrix ($\lambda_s = \lambda_d = 0$ s) is included for reference. It is observed that the drop deforms more as its relaxation time increases. The case of a Newtonian drop placed in a viscoelastic fluid ($\lambda_d = 0$, $\lambda_s \neq 0$) leads to an opposite trend (not shown). Deformation is shown to increase with time. The case of small relaxation time (0.01 s) is also included in the figure. Although this value of the relaxation time is small the figure shows that there is a significant difference between Newtonian and viscoelastic systems.

The fact that fluid elasticity enhances deformation is somewhat surprising, as one expects elasticity to oppose deformation (one can easily picture the stretching of an elastic band to be

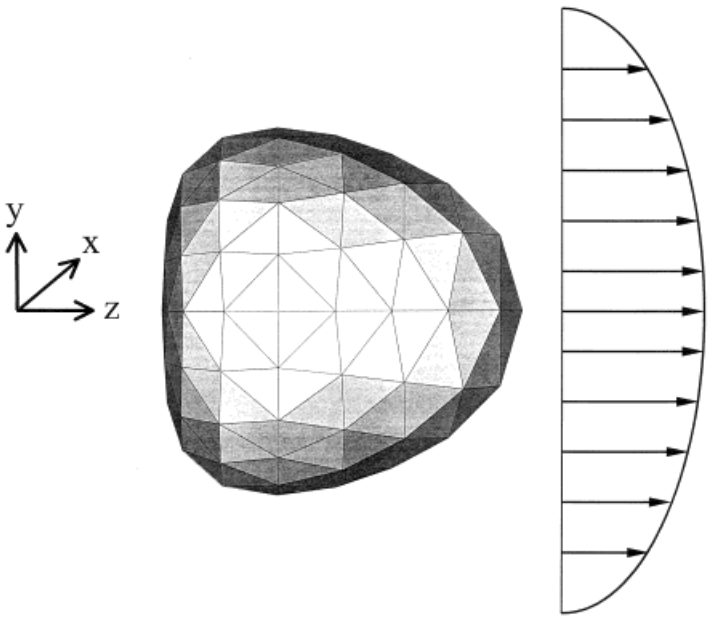

Figure 12. Typical deformation of a three-dimensional drop subject to ambient (cylindrical) duct flow. The figure shows the type of mesh used and co-ordinate systems.

more difficult than that of a liquid band!). However, the results shown in Figure 15 are based on a *linear* (Maxwell) constitutive model, which reflects the true fluid behavior under conditions of small deformation rates only. To illustrate the role of elasticity more clearly, consider the discretized form of the Maxwell constitutive equation, which is Equation (7) with $\eta^{(s)} = 0$. For simplicity of discussion, the subscripts and superscripts are dropped. Thus, for the drop, the constitutive equation becomes

$$\lambda \frac{\partial \tau}{\partial t} + \tau = \eta \Delta \tag{39}$$

Here λ and η should be understood as the relaxation time and viscosity of the drop respectively. If the transient term is approximated by implicit finite difference, then at the kth step, it is not difficult to show that, to $O(\Delta t)$, the excess stress tensor is given by

$$\tau^{(k)} = \eta \alpha \sum_{i=0}^{k} \left(\frac{\lambda \alpha}{\Delta t} \right)^{i} \Delta^{(k-i)} \tag{40}$$

where $\alpha = [(\lambda/\Delta t) + 1]^{-1}$ is given similarly as in Equation (31). Now, the rate-of-strain tensor is assumed to remain essentially unchanged with time, such that $\Delta^{(k)} \approx \Delta$. This is a reasonable

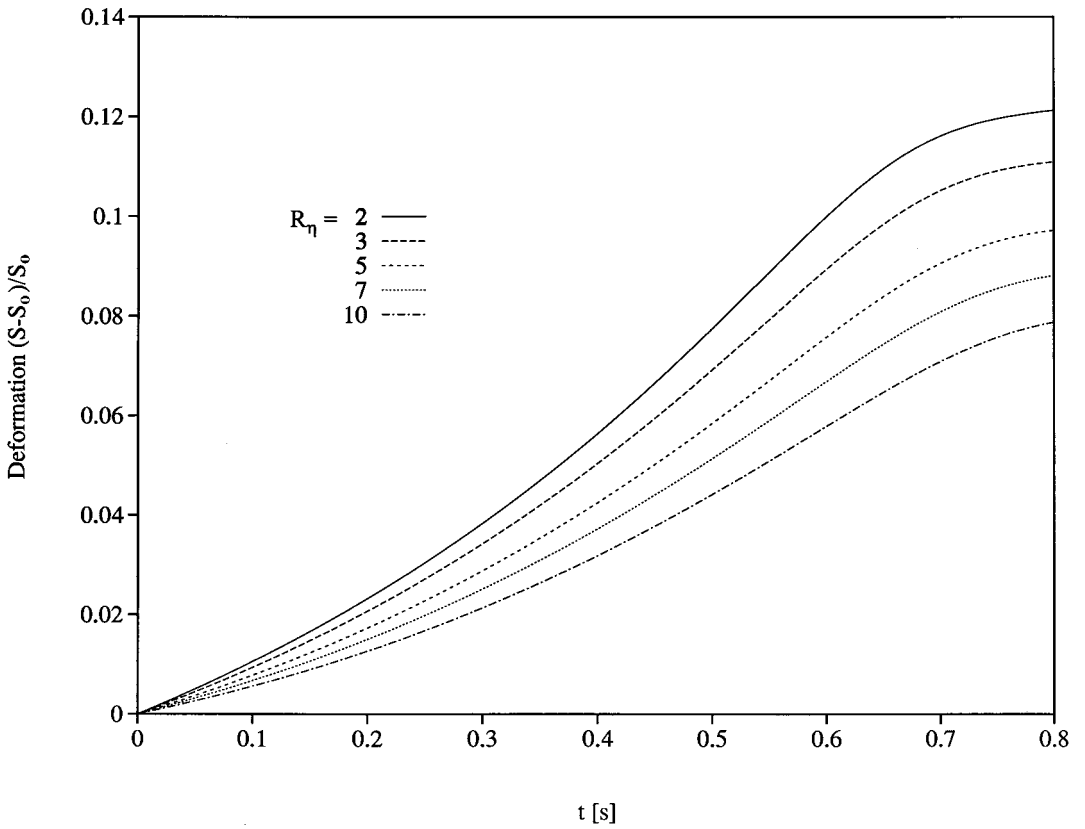

Figure 13. Influence of viscosity ratio on drop deformation for $R_\eta \in [2, 10]$. Both drop and suspending fluid are Newtonian ($\lambda_d = 0$ and $\lambda_s = 0$) and $\gamma = 1$ dyn cm^{-1}.

assumption in the current problem of a drop deforming in a duct flow, where the mean of the rate-of-strain tensor corresponds to fully developed Poiseuille flow. In this case, since $|\lambda\alpha/\Delta t| < 1$, Equation (40) reduces to

$$\tau^{(k)} = \eta\alpha \sum_{i=0}^{k} \left(\frac{\lambda\alpha}{\Delta t}\right)^i \Delta^{(k-i)} \approx \left[\eta\alpha \sum_{i=0}^{k} \left(\frac{\lambda\alpha}{\Delta t}\right)^i\right]\Delta = \eta\alpha^2\Delta \tag{41}$$

for large k. Note that the Newtonian limit is recovered from Equation (41) when $\lambda = 0$. Equation (41) clearly indicates that the effective viscosity for a viscoelastic fluid is approximately equal to $\eta\alpha^2$, and is therefore smaller than the Newtonian viscosity. Since drop deformation increases for drops with smaller viscosity, this explains why a viscoelastic drop

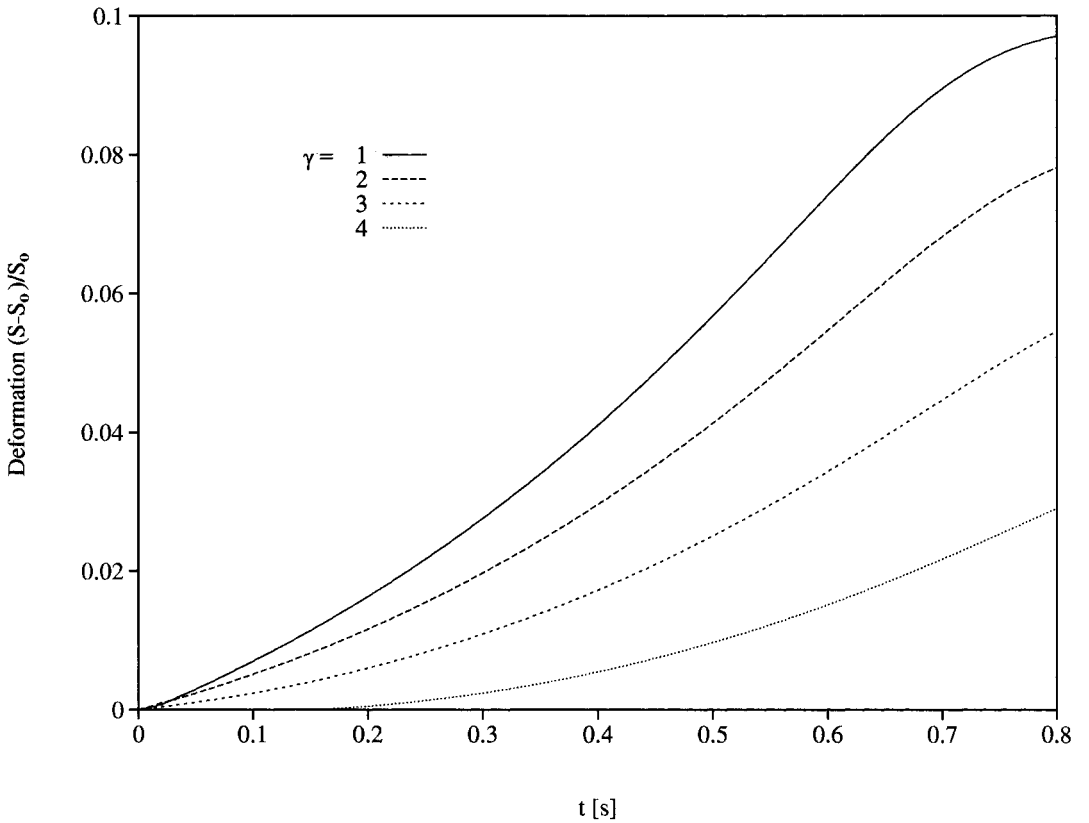

Figure 14. Influence of interfacial tension on drop deformation for $\gamma \in [0, 4]$ (dyn cm^{-1}). Both drop and suspending fluid are Newtonian ($\lambda_d = 0$ and $\lambda_s = 0$) and $R_\eta = 5$.

tends to deform more than a Newtonian drop (with the same viscosity) or a drop with higher relaxation time.

The results in Figure 15 are in agreement with the findings of Bousfield *et al.* [58], who considered the break-up of viscoelastic filaments. They followed the evolution of an imposed disturbance on a filament of dilute polymer solution obeying the Oldroyd-B constitutive equation using a transient finite element solution and a one-dimensional thin filament approximation. They found that the disturbance initially grows much more rapidly on the viscoelastic filament (see Figure 9 in the paper by Bousfield *et al.* [58]). This behavior is in compliance with linear theory. These observations also correlate well with the finite element calculations of Mao and Khayat [37] in the case of the deformation of a viscoelastic liquid column.

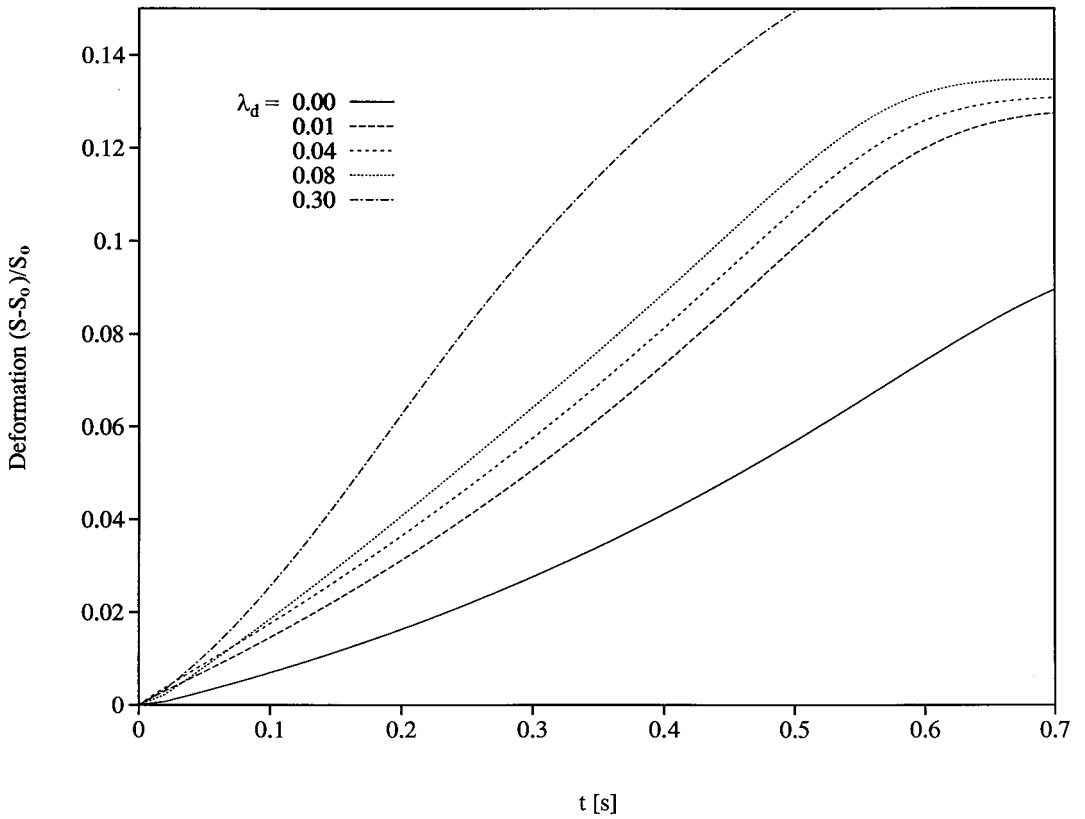

Figure 15. Influence of fluid elasticity for a viscoelastic drop deforming in a Newtonian suspending fluid for $\lambda_s = 0$ and $\lambda_d \in [0, 0.3]$ (s), $\gamma = 1$ dyn cm^{-1} and $R_\eta = 5$.

6. CONCLUDING REMARKS

A boundary element approach is proposed for the analysis of three-dimensional drop deformation in a confined medium of viscoelastic fluid systems obeying the linear Oldroyd-B or Jeffrey's model. A boundary-only formulation is implemented for this constitutive model. A Lagrangian formulation is adopted for the evolution of the interface between drop and suspending fluid. As the triangular boundary element mesh becomes distorted with time, the stretched elements are sub-divided into two elements once the longest edge exceeds an imposed criterion for length. At each node of the mesh the curvature is determined in an average sense, thus allowing the account of interfacial tension. The validity of the method is first established upon comparison with exact results in the case of two-phase viscoelastic rotating flow around a rigid sphere. The influence of mesh size and mesh refinement on the accuracy and convergence of the formulation is assessed for the case of a three-dimensional drop deforming

in simple shear flow. The accuracy is examined by monitoring the evolution of the relative change in drop volume. Obviously, any change in volume is a measure of numerical error. It is demonstrated that the error can be controlled to any degree of accuracy through mesh refinement. Finally, the influence of the viscosity ratio, interfacial tension and drop elasticity is explored for a three-dimensional drop deforming inside a cylindrical duct. While drop viscosity and interfacial tension inhibit deformation, drop elasticity tends to enhance deformation.

The observation that fluid elasticity enhances deformation is in agreement with the findings of existing solutions on free surface deformations of viscoelastic fluids. The range of validity of the present formulation is obviously limited to small rates of deformation. As the rate of deformation increases with motion, non-linear normal stresses (which lead to the Weissenberg rod-climbing phenomenon) become significant enough to oppose deformation. A natural and important extension of the present study is to include the upper-convected terms in the constitutive equation for an adequate account of non-linear normal stress effects.

REFERENCES

1. Khayat RE, Derdouri A, Frayce D. Boundary element analysis of three-dimensional transient mixing flows of Newtonian and viscoelastic fluids. *International Journal for Numerical Methods in Fluids* 1998; **28**: 215.
2. Khayat RE. A boundary element analysis of 3D multiply-connected cavity mixing of polymer solutions. *International Journal for Numerical Methods in Fluids* 1999; **31**: 1173.
3. Khayat RE. A three-dimensional boundary element approach to confined free-surface flow as applied to die casting. *Engineering Analysis of Boundary Elements* 1998; **22**: 83.
4. Khayat RE, Marek K. An adaptive boundary element Lagrangian approach to 3D transient free-surface flow of viscous fluids. *Engineering Analysis of Boundary Elements* 1999; **23**: 111.
5. Khayat RE, Derdouri A, Hebert LP. A boundary element approach to three-dimensional gas-assisted injection molding. *Journal of Non-Newtonian Fluid Mechanisms* 1995; **57**: 253.
6. Khayat RE, Raducanu P. A coupled finite element/boundary element approach for the three-dimensional simulation of air venting in blow molding and thermoforming. *International Journal for Numerical Methods in Engineering* 1998; **43**: 151.
7. Koch CJ, Leal LG. The stability of drop shapes for translation at zero Reynolds number through a quiescent fluid. *Physical Fluids* 1989; **A1**: 1309.
8. Stone HA, Leal LG. Relaxation and breakup of an initially extended drop in an otherwise quiescent fluid. *Journal of Fluid Mechanics* 1989; **198**: 399.
9. Pozrikidis C. The instability of a moving viscous drop. *Journal of Fluid Mechanics* 1990; **210**: 1.
10. Li XZ, Barthes-Bielsel D, Helmy A. Large deformations and burst of a capsule freely suspended in an elongational flow. *Journal of Fluid Mechanics* 1988; **187**: 179.
11. Hiram Y, Nir A. A simulation of surface tension driven coalescence. *Journal of Colloid Interface Science* 1983; **95**: 462.
12. Pozrikidis C. The axisymmetric deformation of a red blood cell in a uniaxial straining Stokes flow. *Journal of Fluid Mechanics* 1990; **216**: 231.
13. Zinemanas D, Nir A. On the viscous deformation of biological cells under anisotropic surface tension. *Journal of Fluid Mechanics* 1988; **193**: 217.
14. Sherwood JD. Breakup of fluid droplets in electric and magnetic fields. *Journal of Fluid Mechanics* 1988; **188**: 133.
15. Rallison JM. The deformation of small viscous drops and bubbles in shear flows. *Annual Reviews in Fluid Mechanics* 1984; **16**: 45.
16. de Bruijn RA. Deformation and breakup of drops in simple shear flows. PhD Thesis, Technische Universiteit Eindhoven, 1989.
17. Rallison JM, Acrivos A. A numerical study of the deformation and burst of a viscous drop in an extensional flow. *Journal of Fluid Mechanics* 1978; **89**: 191.
18. Youngren GK, Acrivos A. On the shape of a gas bubble in a viscous extensional flow. *Journal of Fluid Mechanics* 1976; **76**: 433.

19. Stone HA, Leal LG. Relaxation and breakup of an initially extended drop in an otherwise quiescent fluid. *Journal of Fluid Mechanics* 1989; **198**: 399.
20. Pozrikidis C. The deformation of a liquid drop moving normal to a plane solid wall. *Journal of Fluid Mechanics* 1990; **210**: 10.
21. Ascoli EP, Dandy DS, Leal LG. Boundary-driven motion of a deformable drop toward a planar wall at low Reynolds number. *Journal of Fluid Mechanics* 1990; **213**: 287.
22. Yiantsios SG, Davis RH. On the buoyancy-driven motion of a drop towards a rigid or deformable interface. *Journal of Fluid Mechanics* 1990; **217**: 547.
23. Martinez MJ, Udell KS. Axisymmetric creeping motion of drops through circular tubes. *Journal of Fluid Mechanics* 1990; **210**: 565.
24. Pozrikidis C. *Boundary Integral and Singularity Methods for Linearized Viscous Flow*. Cambridge University Press: Cambridge, 1992.
25. Tsai TM, Miksis MJ. Dynamics of a drop in a constricted capillary tube. *Journal of Fluid Mechanics* 1994; **274**: 197.
26. Kim S, Karrila SJ. *Microhydrodynamics: Principles and Selected Applications*. Butterworth: London, 1990.
27. Stone HA. Dynamics of drop deformation and breakup in viscous fluids. *Annual Review of Fluid Mechanisms* 1994; **26**: 65.
28. Power H, Wrobel LC. *Boundary Integral Methods in Fluid Mechanics*. Computational Mechanics Publications: Southampton, 1995.
29. Khayat RE, Luciani A, Utracki LA. Boundary element analysis of planar drop deformation in confined flow. Part I. Newtonian fluids. *Engineering Analysis of Boundary Elements* 1997; **19**: 279.
30. Khayat RE, Luciani A, Utracki LA. Boundary element analysis of planar drop deformation in confined flow. Part II. Viscoelastic fluids. *Engineering Analysis of Boundary Elements* 1998; **22**: 291.
31. Khayat RE, Huneault M, Utracki LA, Duquette R. A boundary element analysis of planar drop deformation in screw channel of a mixing extruder. *Engineering Analysis of Boundary Elements* 1998; **21**: 155.
32. Bourry D, Godbille F, Khayat RE, Luciani A, Picot J, Utracki LA. Extensional flow of polymeric dispersions. *Polymer Engineering Science* 1999; **39**: 1072.
33. Khayat RE, Luciani A, Utracki LA, Godbille F, Picot J. Influence of shearing and elongation on the deformation of drops in a convergent/divergent tube of Newtonian and viscoelastic fluids. *International Journal of Multiphase Flow* 2000; **26**: 17.
34. Khayat RE. Deformation of a shear-thinning drop in Newtonian flow. *International Journal for Numerical Methods in Fluids* 2000; **33**: 559.
35. Khayat RE, Garcia-Rejon A. Uniaxial and biaxial unsteady inflation of a viscoelastic material. *Journal of Non-Newtonain Fluid Mechanics* 1992; **43**: 31.
36. Khayat RE. A perturbation approach to planar flow of a viscoelastic fluid with two moving free boundaries. *Quarterly Journal of Mechanics and Applied Mathematics* 1994; **47**(3): 342.
37. Mao W, Khayat RE. Numerical simulation of transient planar flow of a viscoelastic materials with two moving free surfaces. *International Journal for Numerical Methods in Fluids* 1995; **21**: 1137.
38. Wrobel LC. The dual reciprocity boundary element formulation for nonlinear problems. *Computer Methods and Applied Mechanics in Engineering* 1987; **65**: 147.
39. Frayce D, Khayat RE. A dual reciprocity boundary element approach to three-dimensional transient heat conduction as applied to materials processing. *Numerical Heat Transfer* 1996; **A29**: 243.
40. Tran-Cong T, Phan-Thien N. Three-dimensional study of extrusion processes by boundary element method. II. Extrusion of a viscoelastic fluid. *Rheology Acta* 1988; **27**: 639.
41. Tanner RI. *Engineering Rheology*. Oxford University Press: Oxford, 1988.
42. Nowak AJ. Application of the multiple reciprocity method for solving nonlinear problems. In *Advanced Computational Methods in Heat Transfer II*, *Vol I: Conduction*, *Radiation and Phase Change*, Wrobel LC, Brebbia CA, Nowak AJ (eds). Computational Mechanics Publications: Southampton, 1995.
43. Neves AC, Brebbia CA. The multiple reciprocity boundary element method for transforming domain integrals to the boundary. *International Journal for Numerical Methods in Engineering* 1991; **31**: 709.
44. Bird RB, Armstrong RC, Hassager O. *Dynamics of Polymeric Liquids* (2nd edn), vol. 1. Wiley: New York, 1987.
45. Rizzo FJ, Shippy DJ. An application of the corresponding principle of viscoelastic theory. *SIAM Journal of Applied Mathematics* 1971; **21**: 321.
46. Kusama T, Mitsui Y. Boundary element method applied to linear viscoelastic analysis. *Applied Mathematics Modelling* 1982; **6**: 285.
47. Christensen RM. *Theory of Viscoelasticity* (2nd edn). Pergamon: Oxford, 1982.
48. Bland DR. *Theory of Linear Viscoelasticity*. Pergamon: Oxford, 1960.
49. Gross B. *Mathematical Structure of the Theory of Viscoelasticity*. Hermann: Paris, 1968.

50. Read WT. Stress analysis for compressible viscoelastic materials. *Journal of Applied Physics* 1950; **21**: 671.
51. Sips R. General theory of deformation of viscoelastic substances. *Journal of Polymer Science* 1951; **9**: 191.
52. Brull MA. A structural theory incorporating the effect of time-dependent elasticity. In *Proceedings of the 1st Midwestern Conference on Solid Mechanisms*, 1953; 141.
53. Lee EH. Stress analysis in viscoelastic bodies. *Quarterly in Applied Mathematics* 1995; **13**: 183.
54. Floryan JM, Rasmussen H. Numerical methods for viscous flows with moving boundaries. *Applied Mechanics Review* 1989; **42**: 323.
55. Batchelor GK. *Introduction to Fluid Dynamics*. Cambridge University Press: Cambridge, 1967.
56. Nambiar RV, Valera RS, Lawrence KL. An algorithm for adaptive refinement of triangular element meshes. *International Journal for Numerical Methods in Engineering* 1993; **36**: 499.
57. Rosenberg G, Stenger F. A lower bound on the angles of triangles constructed by bisecting the longest edge. *Mathematics and Computing* 1975; **29**: 390.
58. Bousfield DW, Keunigs R, Marrucci RG, Denn M. Nonlinear analysis of the surface tension driven breakup of viscoelastic filaments. *Journal of Non-Newtonian Fluid Mechanics* 1986; **21**: 79.

